THE VIKING INORGANIC ANALYSIS EXPERIMENT: INTERPRETATION FOR PETROLOGIC INFORMATION

by

MARC MATTHEW MADERAZZO

S.B., Massachusetts Institute of Technology
(1976)

SUBMITTED IN PARTIAL FULFILLMENT
OF THE REQUIREMENTS FOR THE
DEGREE OF

MASTER OF SCIENCE

at the

MASSACHUSETTS INSTITUTE OF TECHNOLOGY

JUNE, 1977

Signature of Author.....
Department of Earth and Planetary Sciences, June 1977

Certified by.....
Thesis Supervisor

Accepted by.....
Chairman, Departmental Committee

Pg. 39 isn't missing. This is a author mis-numbering error.

THE VIKING INORGANIC ANALYSIS EXPERIMENT:

INTERPRETATION FOR PETROLOGIC INFORMATION

by

MARC MATTHEW MADERAZZO

Thesis Supervisor: Roger G. Burns, Professor of Geochemistry

Submitted to the

Department of Earth and Planetary Sciences

on May 12, 1977,

in partial fulfillment of the requirements for the Degree of

Master of Science

ABSTRACT

The x-ray fluoresence experiment aboard Viking Lander #1 provides data on elemental abundances in soil samples taken from Chryse Planitia. Proportions of oxides are calculated for the lowest oxidation states of the cations reported. Petrologic inferences and the chemical models of Huguenin (1973a,b, 1974, 1975, 1976a,b) permit extrapolation of undetectable sodium. This new chemical analysis is postulated to be approximately isochemical to that of the precursor to the material analyzed. A modified C.I.P.W. normative mineralogy is calculated. An olivine picrite is proposed as a typical Martian dark-area assemblage. The photochemical weathering products of this assemblage are calculated according to the model of Huguenin et al. (1977b). These calculated mineralogies are compared with those of Baird et al. (1976). A parent-daughter relationship is demonstrated between the proposed Martian mantle mineralogy of Johnston et al. (1974) and the calculated precursor on the basis of petrologic arguments. Samples representative of the calculated primary material and photochemical weathering products are prepared for laboratory measurement of visible and near-infrared relectance spectra. Microprobe analysis of some samples is performed. Laboratory reflectance spectra are compared with remotely-sensed spectra of Mars measured by McCord et al. (1977a). It is concluded that the assumptions made earlier are consistent with available data, and a method is thus indicated for remotely and indirectly assessing bulk mineralogies in simple chemical systems with significant accuracy.

TABLE OF CONTENTS

DEDICATION

This thesis is dedicated with love to my parents, Matthew and Marie, for their constant support and good advice. Thanks for our years together, and for trying to teach me so much that I could only understand later.

I. INTRODUCTION

The surface of Mars exhibits significant regional variation in terms of albedo and topographic relief. An unknown, presumably moderate, degree of geologic diversity underlies the many regional features mapped by Mariner 9 (1971) and Viking I and II (1976).

Approximately three quarters of the Martian surface is covered with deposits of extremely fine-grained (1-2 μm) high albedo dust. Huguenin (1973a, b; 1974; 1976 a, b) and Huguenin et al. (1977b) proposed that this dust is the photochemical weathering product of coarse-grained Fe^{2+}- and Ca^{2+}-rich soils which are believed to comprise the areally subordinate low-albedo areas[1,2,3]. The photochemical weathering process is surface-controlled and stimulated by ultraviolet radiation. The rate at which weathering proceeds varies locally with composition and particle size. A detailed discussion of the mechanisms constituting the overall process is given by Huguenin et al. (1977b). Under contemporary conditions, assuming 25% of the surface to be covered with the coarse-grained soils of basaltic to ultrabasic material, the alteration rate is calculated as 10^{-3} to 10^{0} μm-year^{-1} [4]. Thus, a maximum of roughly 1 km of altered regolith may be present, so that primitive basalt flows would be expected to alter to fields of chemically-etched boulders and dust.

Viking lander number 1 touched down in the Chryse Planitia region (at 22.49N, 48.01W), on the mutual boundary

of a large, high-albedo area and a smaller dark region. The ideal soil sample at this site is expected to contain both primary and altered soils. In reality, it is unlikely that any given sample will resemble such an idealization. There is evidence that efficient segregation takes place between the two components[5,6].

The landing site appears to display several indications of geologic variation: pitted and unpitted rocks of low-to-high color indices, dune-like eolian deposits, numerous bedrock outcrop exposures, and perhaps a mafic dike[7] are present. Three surface samples were secured by VL-1 for distribution among the various internal experiments. The principal investigator, Toulmin, believes the Inorganic Analysis Experiment to have received a mixture of eolian fines and coarser, pebble-like rock fragments. The chemical analysis of these materials was performed by an automated energy-dispersive x-ray fluorescence spectrometer. Four sealed, gas-filled proportional counters detect the x-ray emissions of surface samples which have been irradiated with ^{55}Fe and ^{109}Cd sources. The output of the counters is processed by pulse-height analysis in order to resolve in detail the features of the spectra. The spectrometers are insensitive to elements for which $Z>12$ [8]. Therefore, the total proportions of all elements lighter than Mg are determined from the raw data as a function of the total intensity of backscattered x-rays, and this quantity is report-

ed as "0" in the analysis. The "0" number represents principally the species O, Na, C, and N. The mean atomic weight of this unresolvable quantity is determined from the ratio of the Compton-scattered and coherently-scattered components of the backscattered primary beam. The mean weight contributions of the detectable heavier elements are then subtracted away to leave the net contribution of the lighter elements[9].

The resulting analyses characterize the surface materials in terms of elemental composition. We recast the analyses in terms of molecular proportions of each element detected. Oxide components are calculated for each cation in its principal oxidation state. Bulk chemistry, excepting overall oxidation state, should resemble that for a planetary-average surface rock. Inferences must be drawn from indirect data[10,11] in order to deduce the specific weathering products to be anticipated. After correction for undetectable sodium, the "0" may be used to impose a constraint upon the total proportion of weathering material present.

A development of the present study is that the results of the Viking Gas Exchange Experiment require a minimum of only 0.1% primary material to explain the observed reactive effects in terms of the photochemical model of Huguenin et al. (1977b).

II. A MODEL OF THE MINERALOGY OF THE MARTIAN SURFACE

A. Photochemical Weathering on Mars

Rocks are classified on the bases of mineralogy and texture. Rarely does knowledge of a modal or normative petrology alone permit the definition of a unique paragenesis for the rock in question. Textural evidence is provided by the VL-1 Imaging Experiment, which permits us to examine the specific sample under consideration, and observe its original field orientation and relationships. Panoramic color imagery of the landing site supports later assumptions concerning Martian petrology.

Ambiguity in the nature of the sample is also introduced when the effects of weathering are considered. Eolian abrasion, nonisochemical metasomatism, and thermal metamorphic effects may obscure or obliterate the original texture of the pristine rock. The chemistry of alteration products formed by weathering are derived below in light of the work of Huguenin et al. (1977b) and Huguenin (1973a,b; 1974). Metamorphic effects are not considered herein.

Four heterogeneous weathering mechanisms affect the overall mineralogy of surface materials on Mars:

1) The oxidation of magnetite (Fe_3O_4) to form hematite (α-Fe_2O_3) and maghemite (γ-Fe_2O_3) proceeds in five steps: a) the disruption of the protective oxide coating on a magnetite grain by adsorbed H_2O. The adsorbed H_2O also

promotes the migration of subsurface cations to the surface through the penetration of H^+ into the substrate, and also by the creation of an extremely efficient hydroxyl ion concentration at the grain surface.

b) H_2O is desorbed at sunrise by solar UV radiation ($\lambda \leq 0.35$ μm), while atmospheric O_2 collisionally dissociates to form physically adsorbed O,

$$O_{2(g)} \rightarrow 2\ O_{(ads)}$$

and a steady state is established by

$$2\ O_{(ads)} + h\nu \rightarrow O_{2(g)}$$

Other species compete in a similar manner for the available adsorption sites:

$$M_{(g)} \rightarrow M_{(ads)}$$

$$M_{(ads)} + h\nu \rightarrow M_{(g)}$$

c) UV illumination causes photoejection of an electron from Fe^{2+}:

$$Fe_3O_4 + h\nu \rightarrow Fe_3O_4^+ + e_p^-$$

These electrons are bound to adsorbed O, leading to adsorbed (physisorbed) O^- ions:

$$O_{(ads)} + e_p^- \rightarrow O^-_{(ads)}$$

d) A second photoelectron is acquired by O^- to form adsorbed O^{2-}:

$$O^-_{(ads)} + e_p^- \rightarrow O^{2-}_{(ads)}$$

These coordinate with ferric iron ions at the surface (photo-

ionized Fe^{2+}) to form ferric oxide:

$$O_{(ads)}^{2-} + 2Fe_3O_4 + [3a\ \alpha\text{-}Fe_2O_3 + 3(1-a)\ \gamma\text{-}Fe_2O_3]$$

e) Since the hematite structure is more closely packed than the magnetite structure, the ferric oxide scales soon fail mechanically, thus exposing fresh magnetite to UV and atmospheric O_2.

2) The alteration of ferromagnesian silicates is similar in general to (1). The principal distinctions are in the relative importance of cation migration and eolian abrasion. In magnetite weathering, adsorbed H_2O is required only at the outset of oxidation (step a); eolian abrasion is unnecessary due to the scale formation process. Conversely, the production of Fe_2O_3 and residual clay from ferromagnesian silicates requires constant reexposure of fresh Fe^{2+}-bearing crystal faces by eolian abrasion, or steady state replenishment of the cations from the bulk of the grain by cation migration. In this case, it is necessary that H_2O be present for extended periods of time (on the order of 10^2 days) in the adsorbed state for migration to be efficient. The binding energy of a proton in a typical lattice site is greater than that for cations of the more common rock-forming species. As a result, cations which vacate their coordination sites do so irreversibly in the presence of inward-migrating protons. A single proton is incorporated per cation site, and the result is the formation of a cryptic kaolinite or beidellite in the bulk of the grain, while ferric oxide forms at the grain surface.

3) The formation of calcium carbonate may occur when CO_2 or $CO + 1/2\ O_2$ adsorb adjacent to a surface site which is occupied by Ca^{2+}. The adsorbed species recombine efficiently with one lattice oxygen to form CO_3^{2-} [12,13,14,15,16]. The role of lattice was confirmed by Eischens and Pliskin (1962) from infrared absorption experiments. The carbonate ion is a reactive intermediate for the buffering of atmospheric CO_2 when the Fe^{2+} cation is present[17]. The formation of $MgCO_3$ is also thought to be negligible[18,19]. Whether CO_2 or $CO + 1/2\ O_2$ dominates in carbonate formation is not understood at present. The efficient recombination of Ca^{2+} and CO_3^{2-} has been widely observed, and was first identified in heterogeneous reactions by Rowland and Lewis (1951).

4) The final relevant mechanism is that for residual clay formation, mentioned above. It is the corrolary process of ferromagnesian silicate weathering to form hematite. The replacement of Fe^{2+} and Ca^{2+} by H^+ to maintain local charge balance is irreversible due to the very high stability of the proton relative to K^+, Na^+, Ca^{2+}, Mg^{2+}, and Al^{3+}. Measurements of reflectance spectra by Hunt et al. (1972) indicated that the principal component of the Martian dust (air-transported eolian fines) was silicate material. The identification was made on the basis of Si-O restrahlen bands at 8-10 μm in the mid infrared. Spectral curve fitting by Hunt and his colleagues led them to conclude that the silicate phase was a montmorillonite. While Hunt et al. (1970, 1971a), and

Hunt and Salisbury (1970,1971) disagree to some extent with the findings of McCord et al. (1969, 1977a) in confirming the presence of basaltic to ultrabasic material on Mars, we note that the findings of Hunt et al. (1970) as noted above are completely consistent with those very observations when placed in the context of a photochemical weathering process such as we have presented.

B. Interpretation of VL-1 Inorganic Analysis Data

The interpretative procedure described below is iterative in that, at each stage of the process, new information can be taken into account to modify results or procedure, and the preceding work then reconsidered to achieve self consistency. The desired end result is the approximation, in the laboratory, of the principal features of high resolution visible and near-infrared (0.3-1.1 μm) diffuse reflectance spectra of Mars, using mineralogy consistent with the bulk chemistry and other observables of the landing site specimens. It must be understood at the outset that remotely-sensed reflection spectra of 200-400 kilometer diameter spots are weighted averages of polymineralic rock powders and whole crystals, taken over an unknown number of underlying geochemical units. It has been suggested[20,21,22] that Mars exhibits only a moderate degree of differentiation. It is further observed[23,24] that the bright area dust is of uniform composition over the entire planet. These factors appear to increase the likeli-

hood of duplicating the principal features of Martian spectra.

Figure 2 describes three of the samples acquired at the VL-1 site[25]. Table 1 shows approximate weight percent determinations for nine elements in sample S-1, as furnished by the principal investigator, Toulmin[26]. These are expressed in terms of lowest-oxidation state component oxides in Table 2.

It is the hypothesis of Huguenin et al. (1977b) that fine-grained high-albedo eolian deposits represent the photochemical weathering products of the primary Martian crystal material. As such, they are expected[27] to reflect the bulk chemistry of the "average" Martian surface rock. The primary material is suggested to be basaltic to ultrabasic in nature. With this in mind, examination of Table 1 reveals an anomalously high sulfur content for such a rock. In the opinion of Fanale (1976), the Martian regolith represents an irreversible sink for volatile compounds, among them oxides of sulfur. Baird et al. (1976) have deduced that Mars has expelled very little of its inventory of volatiles, so we conclude tentatively that this high value for sulfur reflects a local enrichment in the sense that both the sulfate ions and the cations they coordinate did not originate in the same parcel of material as the other, native phases. One possible mode of origin is during a period of large scale volcanic activity, with particular reference to the giant nearby shield volcanoes, whose present day appearance is quiescent. By analogy with large volcanic eruptions on earth, it is reasonable to assume that

dust and volatiles could circulate on a planetary scale. The Martian atmosphere is capable of supporting high aerosol concentrations for extended periods of time[28].

The mean oxide analysis of S-1 is compared with the pyrolite model of the terrestrial mantle and with two asymptotic models of Martian mantle material in Table 3 (after Johnston et al., 1974). Major discrepancies in alumina, magnesium, and calcium are immediately apparent. This is so because column four describes a crustal composition, while columns one, two, and three refer to mantle compositions. Alumina, silica, iron, and alkalis are generally enriched relative to magnesium and calcium in crustal material versus mantle material[29]. Examination of chemical analyses for rocks of continental tholeiitic provinces, continental deep mafic sources, and orogenic ultramafics reveal several close approximations to the approximate bulk Martian composition. These are presented in Table 4.

Further evidence for deep mafic sources for Martian crustal rocks is seen in the volcanic shields, most notably Nix Olympica (133°W, 018°N). Since the central caldera is elevated 23 kilometers above the mean Martian sphere, the magma source is calculated to lie near 400 kilometers[30] in depth on the basis of hydrostatic considerations. This is twice the depth to the base of the Martian lithosphere[31].

VL-1 imagery[32] tentatively identifies a mafic dike in the middle distance.

At this stage of our discussion let us reconsider Table 2. Table 5 shows Table 2 with sulphur set equal to the mean of analyses 2-6 of Table 4, the balance of sulphur to be considered as foreign to the chemical system of the original primary mineral assemblage. With sodium added as noted above, the analysis is scaled to 100.00 weight percent. This is taken to be the mean weight analysis for the "average" Martian primary crystal rock. Mechanically-pulverized fragments of this material are believed to be[33,34,35] the coarse-grained soils of the dark areas which comprise 25% of the Martian disk.

The next step is to "weather" the average crustal rock with the mechanisms of Huguenin et al. (1977b). This provides us with the planetary average dust composition. The results of the Imagery experiment[36] and Huguenin's interpretation of the Viking Biology experiments[37] imply that the eolian fines, which constitute S-1, contain 98 weight percent or more alteration products. The photochemical weathering scheme implied for a mafic source rock is given in Figure 3. We now develop a specific parent mineralogy consistent with the model discussed above. Slight modifications of the standard C.I.P.W. normative mineralogy[38] are made to facilitate application to the Martian system. Figure 4 lists the steps

of the procedure. A normative mineralogy using the data of Table 5 is shown in Table 7a. The calculated mineralogy of the precursor to S-1 after Baird et al. (1976) appears in Figure 7b. Immediately, a number of questions are raised regarding the self-consistency of the Baird calculation. While this represents a possible stable assemblage under present conditions, there is no evidence of silica-saturated primary rocks on Mars in reflectance spectra[39]. McCord et al. (1969, 1971a, 1972, 1977a) and Adams (1975) find evidence for ubiquitous olivine (fayalite) and/or basaltic glass in dark area reflectance spectra of Mars. These findings are difficult to reconcile with an oversaturated parent material for dust which is found to be homogeneous on a planetary scale. The mineralogy of Baird et al. (1976) is also inconsistent with the concept of a poorly differentiated planet.

Conversely, the normative analysis found by the method of Figure 4 appears petrologically sound, and satisfies the constraints noted above.

C. A Normative Mineralogy for the Average Martian Crustal Rock

Since the XRF experiment cannot distinguish between oxidation states of a given cation, we recalculate FeO as FeO plus Fe_2O_3, based upon an average of the proportions found in analogous terrestrial analyses (Table 4):

$$FeO[0.2686] \rightarrow FeO[0.2186] + Fe_2O_3[0.0250]$$

We recalculate the "O" inventory, and understand that the surplus of "O" beyond that required to form the reduced oxide

phases can be employed later to impose constraints on the volume of weathering phases present in the S-1 sample. These results appear in Table 6.

The application of Figure 4 results in the normative mineralogy presented in Tables 7a and 7b. Let us examine this mineralogy along with that of Baird et al. (1976).

Table 7 describes a rock of generally low albedo dominated by substantial olivine, Fa_{44}, and a normative clinopyroxene, $Wo_{100}En_{56.5}Fs_{43.5}$. Opaque phases constitute approximately ten weight percent of the analysis. Minor nepheline implies some degree of undersaturation, and the plagioclase is seen to lie in the labradorite field, and is expected to occur in the low-temperature structure.

The spectra interpretations of McCord et al. (1969, 1971a, b) and Adams et al. (1969, 1970) reveal indications of strong clinopyroxene band structure at 1 and 2 microns, and the specific composition of the monoclinic pyroxenes varies considerably from one region to another[40].

Huguenin et al. (1977b, in press) predict medium to medium-high anorthite content for plagioclase on the basis of remotely-sensed diffuse reflectance spectra. This also agrees well with the results of the norm calculation.

Examination of reflectance spectra by Huguenin et al. (research in progress) indicates a predominant olivine or basaltic glass phase in the Chryse Planitia region and in general on the Martian surface. This is in agreement with the

work of Adams (1975), and is consistent with the results of the norm calculation.

We have seen that a simple model involving relatively few assumptions (for which support is given) yields a planetary average primary assemblage which is in good qualitative agreement with observation. This assemblage is now weathered by the photochemical mechanisms outlined above, and the resulting alteration phases are tabulated. The surplus "0" may now serve to constrain the total volume of the weathering materials present. The balance of the total above the weathering phases is then attributed to primary material plus sulfate and water (the former is defined, as before, as external to the local geochemical system) to equal 100.00 weight percent. The precise nature of the local primary material at the VL-1 site is more closely approximated on the basis of independent observations by adjustment of the planetary-average primary mineral assemblage.

D. Alteration Phase Assignments

We see in Table 7a the principal saturated phases in a basaltic magma of VL-1 site precursor material, when crystallized at low f_{O_2} as at the Martian surface. We assume, as before, that this assemblage is approximately representative of Martian dark area material. Figure 3 shows schematically those primary phases, and their respective contributions to the various weathering product phases.

Recalling the alteration mechanism for ferromagnesian silicates in Chapter I, we now evoke an entirely analogous mechanism which operates upon the salic phases: an alkali aluminosilicate weathering mechanism which breaks down alkali feldspar. While calcic feldspar contributes to carbonate production by surface recombination of CO + 1/2 O_2 or CO_2 with one lattice oxygen to form $CaCO_3$ at calcium coordination sites, there exists at present no data on recombination kinetics with Group 1 cations. Treatment of albite weathering must therefore remain incomplete. We shall note, however, that migration of alkali metal cations within the lattice under the weathering conditions set out above is favored energetically (see Chapter I). We therefore propose, in addition to the residual Mg-silicate clay described earlier, a residual aluminosilicate clay. It is useful to reflect upon the extremely small dimensions of these clay fragments: 1-10 μm from first principles. One question which lies beyond the scope of this thesis is the possibility of polymerization of these particles (under Martian conditions) to form a Martian analog of antigorite. The physical disposition of the clay phases is, at present, uncertain.

The two intimate clay phases are the principal bulk constituents of the weathering phase material. The differential mobilities of the relevant cations lead in some cases to comparatively complete leaching of cations from the silicate lattice. This is believed to occur in the case of olivine

of high iron content. This leads to the prediction of silica (phase unspecified) in the weathering material.

As noted earlier, hematite (and maghemite) is produced at the expense of magnetite. During scale formation, there is the opportunity for hydration to occur. We therefore expect abundant goethite FeOOH, intermingled with the oxide phases. Similarly, calcic rocks give up Ca^{2+} to form $CaCO_3$ in a heterogeneous reaction.

The operation of the magnetite weathering mechanism on ilmenite gives rise to a TiO_2 phase.

The contribution of these phases to the overall spectra is difficult to assess. The intense absorptions in the spectrum of Fe_2O_3 arise from charge transfers between Fe^{3+} and O^{2-}, as well as from ligand-field transitions involving Fe^{3+} [41,42,43] (see Figure 20).

While pure TiO_2 has no absorption bands (Ti^{4+} has no d-electrons), the presence of impurity iron gives rise to a spectrum. Whereas the spectra of hematite and goethite show intense absorption shortward of 0.6 μm, with subsidiary features at 0.89 and 0.85 μm, respectively, ilmenite shows only a charge-transfer ($Fe^{2+} \rightarrow Ti^{4+}$) band at 0.6 μm; the 0.41 μm feature in rutile is attributed to $O^{2-} \rightarrow Ti^{4+}$ charge transfer.

Clays typically exhibit absorption features near 1.9 μm; this is the $(\nu_2 + \nu_3)H_2O$ band. There are much weaker H_2O bands at 0.95 and 1.15 μm. Sometimes an OH band is visible at 2.34 μm. This overlaps the Fe^{2+} 2.34 μm feature which characterizes many materials.

Carbonate spectra consist largely of vibrational combinations and overtones which reside in the 1.4 to 2.5 μm region. These lie below the detectability levels for our data.

Quartz is detected on the basis of mid-infrared Si-O restrahlen bands. We shall conduct no mid-infrared spectroscopy.

The preparation of samples for laboratory reflectance spectroscopy consisted of locating the best samples of the minerals we required, within the constraints of fiscal practicality. While it was not possible to match each normative phase with a sample for use in the reflectance work, most of the desirable mixture options were covered by the twelve samples (see Table 9) decided upon.

The powders to be used in the spectrometer were hand-ground from pebble-sized crystals and aggregates. Mixtures were intimately combined by grinding of components together, rather than mixing powders. Proportions, determined by the normative procedure or by personal inclination, were meted out on a top-loading digital balance, to within 0.01 g.

Sample 1 is an approximation of the Table 7 normative mineralogy.

Sample 8 is pure weathering product phases, as in Figure 13.

Sample 2 is a 1:10 mixture of samples 1 and 8, and strives to reproduce the major features of the spectra of regions transitional from a higher- to a lower-albedo area, such as

the landing site for VL-1. While the actual admixture ratio could be as low as 1:1000 in theory, the proportion decided upon ensured detection of the pyroxene and olivine spectral features.

E. Microprobe Analysis of Samples for Laboratory Reflectance Spectra

Pyroxene samples were prepared for microprobe analysis. The results are tabulated in Table 8. All samples were ordered from type location specimens through the Ward catalog. Interesting discrepancies between the supposed nature of the individual samples and their actual mineralogy are indicated in Table 8.

A Materials Analysis Corporation Model 5 Electron Microprobe was used for the analysis; the device is a facility of the Department of Earth and Planetary Sciences at MIT. With a reference current of 0.03 μA, the samples were referred to appropriate standards and automated microprobe analysis was performed for seven cations. On the basis of the analyses presented, certain modifications of the intended course of action regarding samples for laboratory spectra were necessitated.

The seven pyroxenes chosen are plotted in the pyroxene quadrilateral in Figure 5. Fassaites I and II plot out of this plane, as in reality do the augites. A subcalcic augite and a fassaite were selected as the pyroxene phases in the model sample for primary dark area material. This is consis-

tent with decreasing the anorthite content given in Table 7 and assigning the SiO_2 and Al_2O_3 thus liberated to fassaite. The CaO alloted originally to feldspar is reassigned then to subcalcic augite. While it is unlikely that these pyroxenes occur together in any specific assemblage, they were selected as most likely to yield reasonable spectra, yet are consistent with the bulk composition and mineralogy of the normative analysis.

The two pyroxene phases thus selected were added in weight proportion to labradorite, magnetite, and ilmenite crystals, and these were ground together to a fine powder. Next, kaolinite, anatase, hematite, calcite, and quartz were combined in the weight proportions of Figure 6. Other pyroxenes were combined with selected phases to provide reference spectra. We discuss the spectra more completely in Chapter XI.

III. A REVIEW OF MARTIAN PETROLOGY

A. The Physical State of Mars

Any detailed investigation of Martian crustal materials necessitates assumptions concerning the thermal evolution of the planet as a whole. While these assumptions are unlikely to define a unique planetary thermal history, the physical constraints imposed by observational data can place limits upon the structure and composition of the interior. A brief review is given below.

Using data from Mariner 9 experiments, Mutch et al. (1976a) determined the mean radius of Mars as 3394 $\pm$ 5 kilometers. Johnston et al. (1974) calculated the moment of inertia factor $I/M\bar{R}^2 = 0.377 \pm 0.001$. This reflects a distinct density increase with depth. As early as 1973, Conrath et al. (1973) reported a weak dipole moment for Mars, further supporting the concept of a dense (metallic) core.

If Mars has a core, virtually all of the planetary material must at one time have been heated above the solidus for whatever core composition we decide upon. The evidence of the Tharsis volcanism implies differentiation, such as may exist at some point, took place early in the planet's evolutionary history[44]. Lewis (1972, 1975) proposed that the Martian core is a eutectic system of Fe and FeS (Fe/FeS = 0.16) with enrichments of heavy alkali metals (though not of sulfur) above their cosmic proportions. This implies the opportunity for significant radiogenic heating episodes to occur due to

the decay of ^{40}K.

Johnston et al. (1974) conclude from the nonhydrostatic state of Mars a lithospheric thickness of about 200 km.

From imagery of the Martian surface (Mariner 4, Mariner 9, VO-1, VO-2), four principal terrains are distinguished (Mutch et al., 1976a): ancient, cratered terrain; younger basalt flows; major volcanic piles including shields and domes, and planet-wide sedimentary (as distinguished from transient features of eolian origin) deposits. A succinct review of Martian crustal evolution is given by Mutch et al. (1976a), which we summarize below:

1) "Cool" accretion, at ≈450°K, approximately 4.6 billion years ago; contemporaneous meteoric bombardment gives rise to the ancient, cratered terrain;

2) Volcanic activity accompanies core differentiation.

3) Tectonic activity and more volcanism as a result of radiogenic heat; extrusions of basalt widespread; intense episodic uplift and subsidence, followed by regional block-faulting and eventual erosion. This is the growth period of the huge shield volcanoes;

4) Completion of the shields; fissure eruptions in the Valles Marineris and continuing tectonic activity;

5) Eolian and photochemical processes rework primitive surface materials; subordinate volcanic and tectonic processes

persist.

Based upon the observations and inferences recapitulated above, Johnston et al. (1974) applied the results of Green and Ringwood's (1969) study of melt behavior in basaltic magmas to the formulation of two self-consistent models of the Martian interior. Both models conclude that the petrology of the Martian mantle is well-described as garnet peridotite. On the basis of the virtually complete absence of characteristic sialic rock features in remotely-sensed dark area reflectance spectra, we agree with Baird et al. (1976), that Mars is likely a poorly differentiated planet. We strenuously disagree with their assignment of a pyroxene-quartz norm for primary crustal materials. The petrologic basis for our reasoning is outlined below. The presence of quartz in the planet-wide alteration product material is accounted for by the photochemical weathering mechanism of Huguenin and co-workers, as described earlier in Chapter II).

The ongoing debate in petrologic circles regarding the origin of the basaltic rocks which constitute the bulk of oceanic and continental crust on earth has given birth to a wide range of viewpoints, each with its supportive evidence. Certain authors, e.g. Yoder (1974), Yoder and Tilley (1957, 1961, 1962), Ito and Kennedy (1967), Kushiro (1968, 1973a, b), and Shairer and Yoder (1961), believe strongly that many rock types are related to basalts by crustal formation and partial melting. The predominance of basalt on earth and Mars then motivates an examination of the origin of these basaltic

magmas. On Mars, we are specifically concerned with possible genetic relationships between the self-consistent mantle composition estimated by Johnston et al. (1974) and the ubiquitous basalt which is detected in remotely-sensed reflectance spectra and confirmed by imagery. In the context of a very limited differentiation sequence as implied by observation, we seek a simple mechanism which identifies a range of basaltic composition from the titanium-rich pyroxenes of spot 24, to the olivine- or iron-rich glass-dominated assemblages of spots 20 and 26 (McCord et al., 1977a), with the proposed garnet peridotite parent material.

Ito and Kennedy (1967) found that garnet lherzolite transformed to a basalt-like assemblage of olivine + clinopyroxene + orthopyroxene + spinel at pressures less than 20 kbar. While the timescale of the experiments did not allow attainment of equilibrium, it is useful to note that plagioclase is absent from the daughter assemblage. Thus, we conclude that lherzolites do not yield the appropriate composition upon melting to form basalt. We should, however, bear in mind that Yoder and Tilley (1962) found that up to 26 weight percent normative anorthite can be accommodated in the normative clinopyroxene molecule. It appears that partial melting of garnet lherzolite depletes the parent in basaltic components only if the liquid is allowed to separate from the crystals (Kushiro, 1973b).

If the imprecisely-known effects of volatiles, deviation of the iron-magnesium ratios from their equilibrium values,

and/or liquid fractionation are qualitatively taken into account, we find (Figure 7) that the liquidus of eclogites and basalts converted to eclogites lie very close to the solidus for garnet peridotite, garnet lherzolite, and spinel lherzolite. Work by Yoder and Tilley (1962), Kushiro (1968), and Yoder (1976) on the joins Fo-An and En-An in the system Fo-CaTs-SiO_2 indicate that parental compositions at X (see Figure 8) yield Fo+En+An after fractionating at Y. Thus, olivine may enter into a reaction relation with pyroxene at depth to yield anorthite. Construction of a flow sheet for the basalt tetrahedron (Yoder, 1976a) shows olivine tholeiite, pheline basanite, and olivine-melilite nephelinite as the immediate parents for the large selection of low-pressure basaltic assemblages enumerated thereon (see Figure 9). These rock types approximate Martian basalts as represented by Table 7. All three immediate parents derive from the same ultimate parent at high pressure, either with or without the presence of volatiles. It is interesting to note that the assemblage of Baird et al. is represented by a daughter of the more primitive assemblages (near point D of Figure 9). Kushiro (1968) has shown that partial melting of garnet peridotite with liquid separation at less than 90 km (28 kb) will exhibit both the olivine reaction relationship above and an ortho-pyroxene reaction relation. On Mars, this will be the case in general throughout the lithosphere. These liquids may proceed to shallower levels to crystallize as olivine basalts.

Migration of the Martian mantle olivine composition from the postaulated Fo_{88} at depth to Fo_{50-56} at the surface reflects simply the melting of olivine to yield a more fayalitic olivine as the melt ascends. This is easily confirmed by examination of the phase relations in Figure unreasonable, within broad limits for f_{O_2}, that an olivine with a specific iron enrichment could yield a magma of the same or lesser iron enrichment upon melting.

B. The Importance of Clinopyroxene in Martian Crustal Petrology

The two existing models of the nominal Martian primary crust contain significant clinopyroxene phases. In the case of Baird et al., the hypothetical precursor to soil sample S-1 (analyzed herein) gives 47 weight percent of a subcalcic augite, $Wo_{14}En_{53}Fs_{33}$ (see Table 7b). We present an analysis (Table 7a) with 23.54 weight per cent clinopyroxene, which we shall nominally refer to as salite, $Wo_{50}En_{28}Fs_{22}$. Figure 11 shows the visible and near-infrared spectra of 6 pyroxenes of the Wo-En-Fs triangle, along with an acmite, $NaFeSi_2O_6$. We note immediately a significant shift in the one-micron feature from salite (3022) to augite (1) and Ti-augite (D2), from 1.155 μm to 1.020 μm. We see that the precise pyroxene composition we select in formulating our analysis will cause a relatively large effect in any laboratory or remotely-sensed spectra of the Martian dark area. We discuss these spectra in a later section.

We consider briefly the paragenesis of clinopyroxenes in the four-component system Di-Hed-Fs-En (Deer et al., 1965) as they relate to the Martian crust. Diopside occurs in picrites and occasionally basalts; salite is the specific pyroxene in hypabyssal rocks of alkali basalt associations; e.g. the Shiant Isles and Black Jack Sill, New South Wales (Turner and Verhoogen, 1960). Hedenbergite occurs in quartz-normative syenites and fayalite granites, as well as in granophyres. This is the pyroxene to be expected in an assemblage like that of Baird et al.. The ferrohedenbergites of the Skaergaard Intrusion (Wager and Deer, 1937) are believed to have inverted from wollastonite solid solution (Deer et al., 1965).

Augite, ferroaugite, subcalcic augite, and subcalcic ferroaugite are the principal ferromagnesian minerals of gabbros, dolerites, and basalts. In tholeiitic rocks, these clinopyroxenes are frequently associated with pigeonite or orthopyroxene, in direct contrast with the subaluminous pyroxenes of the more picritic rock types above. In many flow basalts, the pyroxene of the oldest lamination is diopsidic. The calcium content then decreases in successive flows, yielding first augite and later subcalcic augite.

Fassaite is an aluminum-rich pyroxene, in which the trivalent aluminum cation occupies principally tetrahedral sites. It is found in quartz-free environments, and is commonly a crystallate of aluminous basaltic melts.

Pigeonites are calcium-poor pyroxenes, with 2 percent or less aluminum by weight. Frequently, the unfilled cation sites for Si and Al are occupied by Fe^{3+} and Ti. Homogeneous monoclinic pigeonite occurs only in chilled rocks, and represents an equilibrium phase. In slowly cooled rocks, however, it frequently inverts to orthopyroxene, exsolving the excess calcium component in augite laths.

Titanaugite occurs in the alkali olivine basalt association on earth, and we would reasonably expect its occurrence to be similarly limited on Mars.

We tentatively conclude that salite, augite, or subcalcic augite, with variable amounts of Ti and other minor elements, are the pyroxenes which are likely to be present in primary Martian crust.

C. The Role of Plagioclase Feldspar in Petrology and Spectra of Martian Crustal Material

While the presence of pyroxene in a modal assemblage results in a well-defined reflectance spectrum, the effect of plagioclase feldspar is not so pronounced. The spectra of several feldspars appear in Figure 8, from McCord et al. (1977a).

Plagioclase is the most abundant mineral in the majority of basic and intermediate lavas. In basalts, plagioclase phenocrysts usually show bytownite (An_{70-90}) cores, with more sodic andesine rims (An_{50-70}). We expect then that, while the normative plagioclase composition of a given basalt might be An_{60}, the remotely-sensed reflectance spectra could show an andesine feature at 1.255 μm, with or without a bytownite

feature at 1.306 μm. The detailed spectrum of course depends intimately upon the mode of occurrence of the feldspar crystals. As a result of this ambiguity, we anticipate a general flattening, or washing out, of the spectrum between approximately 1.20 and 1.35 μm, if significant plagioclase is modally present at the surface as noted above, normative plagioclase does not necessarily imply modal plagioclase at the surface in all cases. Some normative plagioclase can be "concealed" in clinopyroxene. Also of interest is the comparatively flat spectrum of perthite in the 1.0 to 1.4 μm range. Perthite is a possible crystallate of sodic assemblages.

Adams (1975) noted that the wavelength of the Fe^{2+} feldspar band, when plotted versus anorthite mole percent, yields the inverse of the 2V versus mole percent anorthite curve. Accordingly, the 2V maximum for low-temperature plagioclase at ≈20% An corresponds to the 1.15 μm short wavelength minimum, and the 2V minimum at 55% An corresponds to the 1.35 μm long-wavelength maximum for this feature. Adams has since refined his technique in estimating the anorthite proportion of plagioclase from reflectance spectra. Since the work was conducted using analyzed samples of terrestrial feldspars, we must conclude that Fe^{2+} is fairly common in substitution. While the ratio of Fe^{3+}/Fe^{2+} for Mars is thought to be higher than that for the earth (Lewis, 1972, 1975), we believe Fe^{2+} may be present in Martian plagioclase.

Petrologically, the role of plagioclase is major. Studies

by Bowen (1928) in the system diopside-albite-anorthite revealed that the presence of diopside lowers crystallization temperatures for plagioclase of a specified composition. It is also a matter of common experience that the pyroxene content tends to increase with the anorthite proportion of plagioclase.

Since melts in this system (see Figure 14) of a composition follows a unique line (the cotectic) across the plagioclase field, we observe that fractional crystallization increases the accessible crystallate compositions relative to the binary system. A rapidly ascending magma of plagioclase-normative composition could crystallize both modal plagioclase and modal olivine at the surface despite the An-Fo reaction relation (Yoder, 1976a). The net effect, once again, is to increase the iron content of olivine (into the hortonolite range) and the calcium content of plagioclase (toward labradorite).

D. Olivine and Basaltic Glass

Olivine is the dominant phase in the normative mineralogy of Table 7a. The discussion in proceeding chapters has touched on the other minerals of possible petrogenic and spectral importance in the Martian regolith. We now discuss olivine, which introduces the greatest single ambiguity into spectral interpretation; we also describe more fully its paragenesis

in basalt. Finally, a review of spectral information regarding basaltic glasses is given to clarify later interpretations.

Orthorhombic olivine exhibits perfect atomic substitution between Mg^{2+} and Fe^{2+} throughout the entire composition range. In nature, no olivines are found in igneous rocks having more than 92 mole percent of the forsterite composition. Such magnesian composition occurs only in dunite. In garnet peridotite, the composition is approximately Fo_{88}. Olivines in basalts are generally restricted to the range Fo_{85} to Fo_{40}. Less frequently, more iron-rich compositions are found in iron-rich dolerites, ferrogabbros, and granophyres. Fayalite occurs with hedenbergite and arfvedsonite in quartz-bearing syenites (Deer et al., 1965) and fayalite ferrogabbros (Carmichael et al., 1974). The classic olivine phase system is reproduced in Figure 10.

Recently, olivine has become central to the debate on the petrology of Mars touched upon earlier: what is the source rock or rocks for Martian melts of basaltic composition? Arguments which were mentioned above present a case for olivine in the source rock for the Martian crust, thought to be garnet peridotite. The reaction relation of olivine with anorthite was also mentioned. Can an olivine basalt such as that of Table 7a (specifically) be derived from the partial melting of a mantle composition suggested by Johnston et al.? If so, will the basalt contain modal olivine when crystallized under 6 millibars of CO_2? The answers to these questions will

affect the uniqueness of our final result, viz., the identification in remotely-sensed Martian reflectance spectra of features characteristic of the assemblage in Table 7a. This corroboration, along with identification of the weathering phases, reflect both upon the accuracy of the normative analysis (Figure 7a), and on the validity of the photochemical weathering scheme we support. If we cannot rule out basaltic glass in favor of olivine from spectral evidence, confirmation of the calculated norm is a more approximate and difficult task.

The positive identification of olivine in reflectance spectra depends upon the positive association of other bands with other phases.

When a few mole percent fayalite are added to forsterite an absorption feature develops at 1.03 μm, which migrates with increasing iron content toward longer wavelengths (Adams, 1975). A pronounced inflection also develops at approximately 1.3 μm. The olivine spectral feature arises from absorptions by Fe^{2+} in M1 (bands at 0.85-0.90 μm and 1.2-1.3 μm) and M2 (bands at 1.04-1.08 μm) lattice sites, and the superposition of these three absorptions gives rise to a broader band than those of pyroxene or plagioclase (Figure 13a). Typically, the Fa content of an olivine cannot be determined more accurately than a 10-20 percent range from reflectance spectra evidence alone. Basaltic glass exhibits a flatter 1 micron feature (Figure 13b) than does olivine, and is less reflective longward of 1 micron.

IV. REFLECTANCE SPECTRA OF MARTIAN ASSEMBLAGES

A. Laboratory Reflectance Spectra

Reflectance spectroscopy of prepared samples was performed at the University of Washington facility; the twelve samples are listed in Table 9. The corresponding spectra appear in Figures 15, 16, 17, 18, and 19.

Immediately we perceive a limitation to our discussion: available telescope spectra cover the wavelength range 0.3 to 1.1 μm, while the laboratory spectra extend approximately from 0.35 to 2.6 μm. We are partially consoled by the identification of persistent H_2O band features at 1.35, 1.88, and 2.10 μm in virtually all spectra. These H_2O bands render difficult to impossible the identification of centers and half-widths for pyroxene "2 μm" features, our principal interest in this region.

If we restrict ourselves to consideration of the 0.35 to 1.1 μm range, we note in Figure 15a a strong absorption just shortward of 0.80 μm. We identify this as an Fe^{2+}-Fe^{3+} charge transfer band. The large feature centered at approximately 1.0 μm arises from an olivine contribution, which causes a flattening effect in the 0.80-0.95 μm region. This is the model normative primary assemblage referred to earlier (Figure 7a).

Figure 15b shows the spectrum of the pale ochre prepared alteration material. The spectra is dominated by the Fe^{2+}-Fe^{3+} charge transfer absorption at 0.85 μm and Fe^{3+}-O^{2-} charge transfer absorption shortward of 0.6 μm. The albedo is

nearly twice that of MM1.

Figure 15c is a 10:1 dilution of MM1 and MM8. The albedo drop is significant (20%), but hematite still dominates the spectrum. Slight flattening between 0.98 μm and 1.1 μm may reflect the strong 1 μm olivine bands seen in Figure 15a.

Figure 16a also shows a well-developed 1 μm feature, but this one is less asymmetric to the short wavelength side. We attribute this to a lesser pyroxene contribution than in MM1. While outside our immediate interests, we note evidence of the 2 μm pyroxene feature in the general flattening of the MM5 curve near the 1.9 μm H_2O band. This is a stronger effect than we noted in Figure 15a. Note also the absence of the short wavelength charge transfer absorption. This sample is of olivine and subcalcic augite, 5:1 by weight.

Olivine plus pigeonite (5:1) in Figure 16b shows a higher albedo than MM5 shortward of 1.5 μm, and a relatively higher albedo above 1.5 μm. The effect of olivine near 1 μm predominates over that of pyroxene. Deeper 2 μm pyroxene bands are noted than in Figure 16a. The inherent asymmetry of the olivine band is clearly in evidence.

Sample MM6 (Figure 17a) shows a salite plus a subcalcic augite. The 1 μm pyroxene band appears broadened, in the range 0.80-1.0 μm. This is likely to be the result of a subcalcic augite band near 0.95 μm and a salite band near 0.90 μm (see Figure 22). There is also an Fe^{2+}-Fe^{3+} charge

transfer band at 0.6-0.75 μm. Once again, 2 μm band structure is nearly obliterated by H_2O.

Figure 17b shows the predictable result of adding wollastonite to the previous sample, MM6.

Figure 17c shows higher albedo than Figure 17a below 1 μm, but is lower above 1 μm. The reproducible deflection of the 1 μm band minimum to just longward of 1 μm is again noted (compare Figures 16a and 16b versus 17a and 17b), and is attributed to the presence of olivine.

As predicted by Adams and McCord (1969) , obsidian in MM10 (Figure 17d) effectively obliterates the spectral features due to olivine and pyroxene, as well as H_2O. Some trace of the charge transfer feature remains.

A reference spectrum of pure fassaite appears in Figure 18a, and of fassaite plus hematite in Figure 18b.

The spectrum of wollastonite is included (Figure 19). It was discovered in the course of investigation that wollastonite is more highly reflective than MgO (the calibration standard), in the visible and near-infrared.

Table 10 lists the features we can identify in our lab spectra with comparative certainty. Analogous spectra to some of those described above were measured by McCord et al. (1976) and appear in Figures 11, 12, 13a, b, and 20.

B. Correlation with Telescopic Spectra

It was hoped initially that better quality spectra would be obtained through use of the University of Washington facility.

Sample impurities, adsorbed and intracrystalline water, and mixing inhomogeneities all could have contributed to the comparative lack of definition in the spectra. It is also important to note that the matching of reflectance spectra even for a single rock is difficult to achieve; the concept of matching a remotely-sensed spectrum of a 200-400 kilometer diameter disk on the surface of Mars with one of only twelve samples is untenable. With this in mind, we cheerfully invite the reader to examine spectra 26, 24, and 22 of Figure 21, for comparison with that of Figure 15c.

Figure 21 are relative spectra, scaled to unity at 0.56 μm to enhance feature resolution. Time constraints did not permit such treatment of the analog spectra which appear in Figures 15, 16, 17, 18, and 19.

We note the same intense absorption between 0.3 and 0.7 μm in both the model and telescope spectra. In both cases, a local maximum is observed to lie just shortward of 0.8 μm. The onset of absorption is noted to take place at approximately 0.78 μm. In a ratioed spectrum, we would also expect the flat behavior of the Figure 21 spectra beyond 0.85 μm to appear in the Figure 15c spectrum.

The immediate implication is, of course, that a generalized basaltic assemblage containing abundant olivine and clinopyroxene can be weathered, and, in intimate association with its photochemical weathering products, will yield a spectrum which largely agrees with those measured for Martian dark areas, where the primary basaltic assemblage is thought to

PAGES (S) MISSING FROM ORIGINAL ?

PG. 39

be "dusted" lightly with the material which so dominates the bright areas.

Comparison of Figure 21 and Figure 15a shows a better correlation, excepting the shoulder at 0.58 μm, which the author believes to be anomalous. We conclude that the bulk mineralogy of spots 22, 24, and 26 consist largely of primary mafic phases, with comparatively little (less than 20%) of the weathering material admixed.

V. CONCLUSIONS

We have considered the Viking inorganic analysis of a sample of eolian fines from the Chryse Planitia region of Mars. Reasoning from the photochemical models of Huguenin et al. (1977b) and the petrologic constraints of Johnston et al. (1974) and Mutch et al. (1976a,b), we modified the inorganic analysis in a simple way to correspond to a possible basaltic precursor to the sample, using a method similar to that employed by Baird et al. (1976). This composition was used as the basis for a conventional normative calculation. The resulting assemblage was examined and found to be a partial-melting product of the proposed Martian mantle assemblage of Johnston et al. (1974). It was further observed that variations exist in basaltic composition sufficient to explain spectral differences observed in the several dark areas of Mars measured by McCord et al. (1977a), and others are derivable in terms of a common parent. Some aspects of this variability were explored in terms of the balance between normative clinopyroxene and modal plagioclase, and samples were then selected for spectral comparison. Microprobe analysis of the expensive sample pyroxenes indicated that we could not model precisely the calculated assemblage, if the work was to be completed within the time available. A partial justification for the choices made is presented. Laboratory reflectance spectra, in analog form, were measured, and found to lack the anticipated detail. Nonetheless, a reasonable spectral match is achieved. Good spectral agreement with so

few samples and relatively few implicit assumptions tends to support (a) the petrologic inferences of the author and others as noted, (b) the photochemical weathering predictions of Huguenin et al. (1977b), and (c), the feasibility of remote petrologic identification to first order using a minimum of (indirect) data.

As the state of our knowledge of Mars improves, it should be possible to repeat this general treatment using better inorganic determinations and better spectra. Only by analyzing many (>100) samples of mixed mineral powders is there a reasonable chance of achieving a perfect or near-perfect match to a specific spot spectrum, or of observing in the laboratory the spectral variation we see in the telescope spectra.

Better control of particle size, and an in-depth analysis of possible metamorphic effects upon the spectra will prove useful. The presence of amphibole is not ruled out by any observations, to date, and it is possible that certain spectra will require amphibole for accurate modelling.

The effects of hydration upon the spectra (e.g. Figure 20) were also neglected, but should eventually be explored.

In conclusion, it is seen that the presence of olivine is important to the explanation of Martian dark area spectra. We, therefore, question the self-consistency of the Baird et al. (1976) calculation of a pyroxene-quartz norm for the sample precursor, and submit instead that the picritic normative mineralogy calculated herein satisfies the constraints we are capable of imposing at present.

ACKNOWLEDGEMENTS

I have many friends to thank for their help in realizing this project.

The speedy and accurate typing of Roxanne Regan is very much appreciated, as were the less successful efforts of my friends Rich Kane and Dave Eckel a few days earlier.

The work would have been a lot less exciting without the fine input of John Dickey on petrologic matters.

Kris Andersen was very helpful in running my spectra for me in Seattle. Mark Sneeringer read large parts of the final draft. Larry Bloomenkranz helped with my logistics problems.

A special word of thanks goes to my thesis advisor, Roger G. Burns. He is a powerhouse of professional expertise in mineralogy and geochemistry, but more importantly, a warm and concerned teacher and friend. I deeply appreciate his help, and I'm proud to have been his thesis student.

Dr. Robert L. Huguenin has been putting up with me since January of 1973. For this alone he deserves a medal. But Bob is much more than a perennial research advisor. He is a good friend and a wise counselor. He's also a very brilliant and original scientist. To round it out, he generates an atmosphere of relaxed good cheer whenever he's around. Somehow I got wired into your research machine, Bob, and I'm thanking you for everything right out here where everyone can see it.

BIBLIOGRAPHY

Adams, J.B., Interpretation of visible and near-infrared diffuse reflectance spectra of pyroxenes and other rock forming minerals, in: Infrared and Raman Spectroscopy of Lunar and Terrestrial Minerals, edited by C. Karr, Jr., Academic Press, New York, 1975.

Adams, J.B. and T.B. McCord, Mars: Interpretation of the spectral reflectivity of light and dark regions, J. Geophys. Res., 74, 4851, 1969.

Adams, J.B. and T.B. McCord, Remote sensing of lunar surface mineralogy: implications from visible and near-infrared reflectivity of Apollo 11 samples, Proc. Apollo 11 Lunar Sci. Conf., 3, 1937-1945 (A.A. Levinson, ed.; Pergamon, New York), 1970.

Baird, A.K., K. Keil, H.J. Rose, Jr., B.C. Clark, and P.T. Toulmin III, Viking and inorganic analysis experiment, Interim Report, submitted to Science 10 November 1976.

Ballhausen, C.J., Introduction to Ligand Field Theory, McGraw-Hill, New York, 298 pp.

Barth, C.A. and C.W. Hord, Mariner ultraviolet spectrometer: Topography and polar cap, Science, 173, 197-201.

Bowen, N.L., The Evolution of Igneous Rocks, Princeton Univ. Press, Princeton, N.J., 332 pp., 1928.

Burns, R.G., Mineralogical Applications of Crystal Field Theory, Cambridge Univ. Press, 224 pp., 1970.

Carmichael, I.S.E., F.J. Turner, and J. Verhoogen, Igneous Petrology, McGraw-Hill, New York, 939 pp., 1974.

Conrath, B., R. Curran, R. Hanel, V. Kunde, W. Maguire, J. Pearl, J. Pirraglia, and J. Welker, Atmospheric and surface properties of Mars obtained by infrared spectroscopy on Mariner 9, J. Geophys. Res., 78, 4267-4278, 1973.

Conrath, B., Thermal structure of the Martian atmosphere during the dissipation of the dust storm of 1971, Icarus, 24, 36-46, 1975.

Cotton, F.A. and G. Wilkinson, Advanced Inorganic Chemistry, Interscience, New York, 1136 pp., 1966.

Deer, W.A., R.A. Howie, and J. Zussman, An Introduction to the Rock-Forming Minerals, Wiley, New York, 1966.

Dell, R.M. and F.S. Stone, The adsorption of gases on nickel oxide, Trans. Faraday Soc., 50, 501-510, 1954.

Eischens, R.P. and W.A. Pliskin, Infrared study of the catalyzed oxidation of CO, Advances in Catalysis, 9, 662-663, 1957.

Fanale, F.P., Martian volatiles: Their degassing history and geochemical fate, Icarus, 28, 179-202, 1976.

Fanale, F.P. and W.A. Cannon, Exchange of adsorbed H_2O and CO_2 between the regolith and atmosphere of Mars caused by changes in surface insolation, J. Geophys. Res., 79, 3397-3402, 1974.

Garner, W.E., The reduction of oxides by hydrogen and carbon monoxide, J. Chem. Soc., 1239-2144, 1947.

Garner, W.E., F.S. Stone, and P.F. Tiley, The reaction between carbon monoxide and oxygen on cuprous oxide at room temperature, Proc. Roy. Soc., A211, 472-489, 1952.

Green, D.H. and A.E. Ringwood, The genesis of basaltic magma, Contrib. Mineral. Petrol., 15, 103-190, 1967.

Hanel, R., B. Conrath, W. Hovis, W. Kunde, P. Lowman, W. Maguire, J. Pearl, J. Pirraglia, C. Prabhakara, B. Schlachman, G. Levin, P. Stratt, and T. Burke, Investigation of the Martian environment by infrared spectroscopy on Mariner 9, Icarus, 17, 423-442, 1972.

Harker, R.I. and O.F. Tuttle, Studies in the system CaO-MgO-CO_2. Part I. The thermal dissociation of calcite, dolomite, and magnesite, Amer. J. Sci., 253, 209, 1955.

Huguenin, R.L., Photostimulated oxidation of magnetite. 1. Kinetics and alteration phase identification, J. Geophys. Res., 78, 8481-8493, 1973a.

Huguenin, R.L., Photostimulated oxidation of magnetite. 2. Mechanism, J. Geophys. Res., 78, 8495-8506, 1973b.

Huguenin, R.L., The formation of goethite and hydrated clay minerals on Mars, J. Geophys. Res., 79, 3895-3905, 1974.

Huguenin, R.L., Mars: Chemical weathering as a massive volatile sink, Icarus, 28, 203-212, 1976a.

Huguenin, R.L., Photochemical weathering and the Viking biology experiments on Mars, Proc. Coll. Water on Plan. Regoliths, Hanover, N.H., October, 1976, 100-106, 1976b.

Huguenin, R.L., T.B. McCord, and J.B. Adams, Mars: Origin of the high albedo materials, paper presented at 55th Annual Meeting, AGU, Washington, D.C., April 8-12, 1974.

Huguenin, R.L., J.B. Adams, and T.B. McCord, Mars: Surface mineralogy from reflectance spectra, Lunar Science VIII, 478-480, 1977a.

Huguenin, R.L., R.G. Prinn, and M.M. Maderazzo, Mars: Photodesorption from mineral surfaces and its effects on atmospheric stability, Icarus (manuscript in press), 1977b.

Hunt, G.R. and J.W. Salisbury, Visible and near-infrared spectra of minerals and rocks: I. Silicate minerals, Mod. Geol., 1, 283, 1970.

Hunt, G.R. and J.W. Salisbury, Visible and near-infrared spectra of minerals and rocks: II. Carbonates, Mod. Geol., 2, 23, 1971.

Hunt, G.R., J.W. Salisbury, and C.J. Lenhoff, Visible and near-infrared spectra of minerals and rocks: IV. Sulphides, Icarus, 13, 226, 1970.

Hunt, G.R., J.W. Salisbury, and C.J. Lenhoff, Visible and near-infrared spectra of minerals and rocks: III. Oxides and hydroxides, Mod. Geol., 2, 195, 1971a.

Ito, K. and G.C. Kennedy, Melting and phase relations in a natural peridotite to 40 kilobars, Amer. J. Sci., 265, 519-538.

Johnston, D.H., M.N. Toksoz, and T.R. McGetchin, The physical state and internal structure of Mars, J. Geophys. Res., 79, 26, 3959-3971, 1974.

Kushiro, I., Compositions of magmas formed by partial zone melting of the upper mantle, J. Geophys. Res., 73, 619-634, 1968.

Kushiro, I., Origin of some magmas in oceanic and circum-oceanic regions, Tectonophysics, 13, 211-222, 1973a.

Kushiro, I., Partial melting of garnet lherzolite from kimberlite at high pressures, in: P.H. Nixon, ed., Lesotho Kimberlites, Lesotho National Development Corp., Maseru, Lesotho, 294-299, 1973b.

Lewis, J.S., Metal/silicate fractionation in the solar system, Earth Planet. Sci. Lett., 15, 286, 1972.

Lewis, J.S., Primordial retention of volatiles by Mars, paper presented at Spring Annual Meeting, AGU, Washington, D.C., 16-19 June, 1975.

Loeffler, B.M., R.G. Burns, and J.A. Tossell, Metal charge transfer transitions: Interpretation of visible-region spectra of the Moon and lunar materials, Proc. Sixth Lunar Sci. Conf., Geochim. Cosmochim. Acta, Suppl. 6,. 3, 2663-2668, 1975.

Loughnan, F.C., Chemical Weathering of the Silicate Minerals, Elsevier, New York, 154 pp.

McCord, T.B. and J.B. Adams, Spectral reflectivity of Mars, Science, 163, 1058, 1969.

McCord, T.B., J.B. Adams, and R.L. Huguenin, Reflection spectroscopy: A technique for remotely sensing surface mineralogy and composition, Orbital Science, NASA-SP (in press), 1977a.

McCord, T.B., J.H. Elias, and J.A. Westphal, Mars: The spectral albedo (0.3-2.5 m) of small bright and dark regions, Icarus, 14, 245, 1971a.

McCord, T.B., R.L. Huguenin, D. Mink, and C. Pieters, Spectral reflectance of Martian areas during the 1973 opposition: photoelectric filter photometry 0.33-1.10 μm, Icarus, 30 (May issue), 1977b.

McCord, T.B. and J.A. Westphal, Mars: Narrowband photometry 0.3-2.4 microns of surface regions during the 1969 apparition, Astrophys. J., 168, 141, 1971.

McCord, T.B. and J.A. Westphal, Two-dimensional silicon vidicon astronomical photometer, Applied Optics, 11, 522-526, 1972.

Mutch, T.A., R.E. Arvidson, J.W. Head III, K.L. Jones, R.S. Saunders, The Geology of Mars, Princeton Univ. Press, Princeton, N.J., 400 pp., 1976a.

Mutch, T.A., A.B. Binder, F.O. Huck, E.C. Levinthall, S. Liebes, Jr., E.C. Morris, W.R. Patterson, J.B. Pollack, C. Sagan, and G.R. Taylor, The surface of Mars: The view from the Viking I lander, Science, 193, 791-801, 1976b.

Nash, D.B. and J.E. Conel, Spectral reflectance systematics for mixtures of powdered hypersthene, labradorite, and ilmenite, J. Geophys. Res., 1615-1622, 1974.

Roland, R.A. and D.R. Lewis, Furnace atmosphere control in differential thermal analysis, Amer. Mineral., 36, 80-91, 1951.

Rudham, R. and Stone, F.S., Chemisorption on cuprous, nickel, and cobaltous oxides. Chemisorption, Proc. Chem. Soc. Symposium, 1956 (edited by W.E. Garner), Academic Press, New York, 205-217, 1957.

Schairer, J.F. and H.S. Yoder, Jr., Crystallization in the system nepheline-forsterite-silica at one atmosphere pressure, Carn. Inst. Wash. Yearbook, 60, 141-144, 1961.

Stone, F.S., R. Rudham, and R.L. Gale, Adsorption and catalysis on cobaltous oxide, Z. Elektrochem., 63, 129-135, 1959.

Tossell, J.A., D.J. Vaughan, K.H. Johnson, The electronic structure of rutile, wustite, and hematite from molecular orbital calculations, Amer. Mineral., 59, 319, 1974.

Toulmin, P.T., III, A.K. Baird, B.C. Clar, K. Keil, and H. Rose, Jr., Inorganic chemical investigations by x-ray fluorescence analysis: The Viking Mars Lander, Icarus, 20, 153-178, 1973.

Turner, F.J. and J. Verhoogen, Igneous and Metamorphic Petrology, 2nd ed., McGraw-Hill, New York, 694 pp., 1960.

Wager, L.R. and W.A. Deer, Geological investigations, in: E. Greenland, Pt. III, The Skaergaard Intrusion, Kangerdlugssung, E. Greenland, Medd. øm. Grønland, 105, 1-352.

White, W.B. and K.L. Keester, Optical absorption spectra of iron in the rock-forming silicates, Amer. Mineral., 51, 774, 1966.

Yoder, H.S., Jr., Generation of Basaltic Magma, National Academy of Sciences, Washington, D.C., 265 pp., 1976.

Yoder, H.S., Jr. and C.E. Tilley, Origin of basaltic magmas: An experimental study of natural and synthetic rock systems, J. Petrol., 3, 342-352, 1976.

Footnotes

[1] McCord et al., 1971a

[2] Adams and McCord, 1969

[3] op. cit., McCord et al. 1971a

[4] Huguenin, 1974

[5] Conrath et al., 1973

[6] McCord et al., 1977a

[7] Mutch et al., 1976b

[8] Toulmin et al., 1972

[9] ibid.

[10] Johnston et al., 1974

[11] Fanale, 1976

[12] Garner, 1947

[13] Garner et al., 1952

[14] Stone et al., 1959

[15] Dell and Stone, 1954

[16] Rudham and Stone, 1959

[17] Huguenin et al., 1977b

[18] op. cit. Huguenin, 1974

[19] Harker and Tuttle, 1955

[20] op. cit., Johnston et al., 1974

[21] op. cit. Mutch et al., 1976a

[22] Baird et al., 1976

[23] op. cit. Conrath et al., 1973

[24] Hunt et al., 1972

[25] op. cit. Baird et al., 1976

[26] op. cit. Toulmin et al.

27 op. cit. Huguenin et al., 1977

28 op. cit. Conrath et al.

29 Carmichael et al., 1974

30 op. cit. Johnston et al. 1974

31 Mutch et al., 1976a

32 op. cit. Mutch et al., 1976b

33 op. cit. McCord et al., 1969

34 McCord et al., 1971

35 op.cit. McCord et al., 1977a

36 op. cit. Mutch et al., 1976a

37 Huguenin, 1976b

38 op. cit., Carmichael et al., 1974

39 op. cit., McCord et al., 1977a

40 Adams, 1975

41 Burns, 1970

42 Tossell et al., 1974

43 Loeffler et al., 1975

44 op. cit. Mutch et al., 1976a

Table Headings

Table 1

Table 1 shows the elemental abundances determined by the VL-1 Inorganic Analysis experiment for the sample S-1. In Tables 1, 2, 5, 6, 7a, and 7b, the column heading "W%" represents the weight per cent of the element or oxide which appears tabulated beneath. The symbol "AW" represents the atomic weight. "MW" represents molecular weight. "MA" is used to represent the molecular amount, or the weight percent divided by the molecular weight, of a particular compound or mineral molecule.

Element	Mean W% $\pm$ SD	AW	Mol. Amt.
Si	18.5-24.0	29.08	$0.7585^{+}_{-}0.0962$
Ti	0.3- 0.5	47.90	$0.0084^{+}_{-}0.0021$
Al	2.0- 5.0	26.98	$0.1297^{+}_{-}0.0556$
Fe	12.5-15.0	55.84	$0.2453^{+}_{-}0.0233$
Mg	2.5- 5.5	24.31	$0.1645^{+}_{-}0.0617$
Ca	3.0- 4.5	40.08	$0.0923^{+}_{-}0.0200$
K	0.0- 0.8	39.09	$0.0102^{+}_{-}0.0102$
S	2.5- 5.0	32.06	$0.1154^{+}_{-}0.0405$
Ce	0.1- 0.7	140.12	$0.0029^{+}_{-}0.0021$
Total	41.4-61.0	-	$1.5272^{+}_{-}0.3117$

Table 2

Table 2 shows the result of assigning oxygen from the large "O" inventory to each of the elements in proportion. This procedure is discussed in the text. Column headings are described on page 54.

Oxide	MA,O	W%,oxide	MW,oxide	MA,oxide
SiO_2	1.5170	45.57	60.08	0.7585
TiO_2	0.0168	0.67	79.90	0.0084
Al_2O_3	0.1946	6.62	101.96	0.0649
FeO	0.2453	17.62	71.84	0.2453
MgO	0.1645	6.63	40.31	0.1645
CaO	0.0923	5.18	56.08	0.0923
K_2O	0.0051	0.48	94.09	0.0051
SO_3	0.3462	9.24	80.06	0.1154
CeO	0.0029	0.45	156.12	0.0029
Total	2.5847	92.46	-	-

Table 3

Table 3 contrasts the pyrolite mantle model of Green and Ringwood (1967), column 1, with the Fe_{85} and FeS martian mantle models of Johnston et al. (1974), columns 2 and 3, and with the mean inorganic analysis from Table 1, column 4.

Oxide	Pyrolite	Fe_{85}	FeS	Mean IA
SiO_2	45.16	39.03	42.32	45.57
Al_2O_3	3.54	3.06	3.32	6.62
FeO	8.04	20.53	13.82	17.62
Fe_2O_3	0.46	0.40	0.43	
MgO	37.47	32.38	35.11	6.63
CaO	3.08	2.66	2.89	5.18
K_2O	0.13	0.11	0.12	0.48
FeO/FeO + MgO	[0.18]	[0.21]	[0.19]	[0.73]
SO_3	-	-	-	9.24

Table 4

Table 4 shows four reasonable approximations to the measured martian surface composition found among analyses of terrestrial basaltic rocks, after Carmichael et al., 1974. Column 1, hedenbergite granophyre, Skaergaard Intrusion, Turner and Verhoogen, 1960; column 2, ferrodiorite, Skaergaard Intrusion, Carmichael et al., p. 477; column 3, melanogranophyre, Skaergaard Intrusion, Carmichael et al., p.477; column 4, picrite basalt, Kilauea, Carmichael et al., p. 714; column 5, mean VL-1 inorganic analysis of S-1.

Table 4

	1	2	3	4	5
SiO_2	47.41	44.10	46.91	47.25	45.57
TiO_2	0.89	2.43	3.54	1.61	0.67
Al_2O_3	8.66	11.70	11.28	9.07	6.62
Fe_2O_3	2.81	2.05	2.13	1.45	-
FeO	11.15	22.68	10.11	10.41	17.62
MnO	0.20	0.21	0.18	0.13	-
MgO	19.29	1.71	7.67	19.96	6.63
CaO	6.76	8.71	9.66	7.88	5.18
Na_2O	1.35	2.95	2.37	1.38	-
P_2O_5	0.43	0.35	1.83	0.35	-
H_2O^+	1.45	0.22	0.80	0.08	-
H_2O^-	0.11	0.20	0.42	0.04	-
Total	100.61	99.16	100.12	99.82	92.46

Table 5

Table 5 is a rationalization of Table 2 in view of petrologic inputs noted in the text. A value has been created for the abundance of undetectable sodium based upon the analyses of Table 4. This quantity appears in brackets to emphasize it's hypothetical origin. Other column headings are defined on page 54.

Element [Oxide]	W%	MA	MW [Oxide]	MA [Oxide]	W% [/scaled]
"O"	46.50	2.9063	-	-	-
Si[SiO_2]	21.00	0.7479	60	0.7479	44.88/48.49
Ti[TiO_2]	0.50	0.0104	80	0.0208	1.66/1.79
Al[Al_2O_3]	4.00	0.1482	102	0.0741	7.56/8.17
Fe[FeO]	15.00	0.2686	71.8	0.2686	19.29/20.25
Ca[CaO]	5.00	0.1123	56	0.1123	6.29/6.60
Mg[MgO]	4.50	0.2262	40	0.2262	9.05/9.47
K[K_2O]	0.80	0.0204	94	0.0102	0.96/1.01
"Na"[Na_2O]	2.65	0.0922	62	0.0461	2.86/3.00
Total	99.95	-	-	-	92.55/100.00

Table 6

Table 6 recapitulates the results of Table 5 in compact form, and includes the value of the "O" inventory (which is described in the text), and the value of surplus "O" is taken to represent that quantity (number of molecules relative to the total number of molecules present in a sample) of "O" which would remain if all cations present were found to be in an oxidized state.

Oxide	MA	W%, scaled
SiO_2	0.7479	48.49
TiO_2	0.0208	1.79
Al_2O_3	0.0741	8.17
Fe_2O_3	0.0250	3.99
FeO	0.2186	15.70
CaO	0.1123	6.60
MgO	0.2262	9.47
K_2O	0.0102	1.01
Na_2O	0.0461	3.00
		98.22
"O"	2.6277	
surplus "O"	0.2787	

Tables 7a and 7b

These two tables present the results of the normative analysis performed according to the reasoning outlined in the text (Table 7a), and that of Baird et al. (Table 7b). The heading of column 2, once again, refers in each case to the weght per cent of each phase noted beneath. The heading of column 1 is in each case self-explanatory.

Table 7a

Primary Equilibrium Phase	W%
olivine Fa_{44}	36.32
diopside	23.54
plagioclase An_{60}	15.02
nepheline	9.11
orthoclase	6.02
magnetite	6.28
ilmenite	3.35
	99.64

Table 7b

Primary Equilibrium Phase		W%
clinopyroxene		47
[wollastonite]	14	
enstatite	53	
[orthoferrosilite]	33	
plagioclase		19
orthoclase		1
magnetite		2
ilmenite		2
troilite (FeS)		8
quartz		21
		100

Table 8

Table 8 appears on the next two consecutive pages. It relates the principal information obtained by electron microprobe analysis of the seven samples as described in the text. "OX" represents the weight per cent of each cation in oxide form. The cations are listed across the top of each article in the Table. "FM" represents the coefficient of the appropriate cation if the chemical formula of the mineral molecule were written out. "Total" is the total of the oxide weight per cents for a given sample. The number below "Total" is the sum of the coefficients as noted above.

Table 8

Sample 1 "pigeonite"

	Fe	Na	Mg	Al	Si	Ca	Ti
OX	11.23	0.18	12.96	2.04	51.84	21.38	0.68
FM	0.176	0.006	0.361	0.045	0.971	0.428	0.009

Conclusion: subcalcic augite — Total 100.31
1.996

Sample 2 "fassaite"

	Fe	Na	Mg	Al	Si	Ca	Ti
OX	7.82	0.03	10.94	12.74	42.95	24.75	0.97
FM	0.245	0.002	0.613	0.565	1.617	0.998	0.026

Conclusion: fassaite — Total 100.20
4.067

Sample 3 "hedenbergite"

	Fe	Na	Mg	Al	Si	Ca	Ti
OX	14.85	0.24	14.80	1.54	53.88	12.12	0.04
FM	0.470	0.018	0.835	0.067	2.042	0.491	0.001

Conclusion: pigeonite or subcalcic augite — Total 97.46
3.924

Sample 4 "wollastonite"

	Fe	Na	Mg	Al	Si	Ca	Ti
OX	0.07	0.02	0.12	0.11	50.54	47.34	0.01
FM	0.002	0.001	0.005	0.004	1.992	1.999	0.000

Conclusion: wollastonite — Total 98.21
4.003

Sample 5 "enstatite"

	Fe	Na	Mg	Al	Si	Ca	Ti
OX	8.89	0.25	15.39	0.82	48.18	23.02	0.14
FM	0.291	0.018	0.897	0.037	1.886	0.964	0.003

Conclusion: salite or diopside — Total 96.67
4.096

Samples 6 and 7 appear on the next page

Table 8, cont'd

Sample 6 "augite"

	Fe	Na	Mg	Al	Si	Ca	Ti
OX	6.21	1.20	14.84	0.86	56.82	22.70	0.00
FM	0.186	0.083	0.790	0.036	2.029	0.868	0.000

Conclusion: Mg-salite or diopside

Total 102.63
3.991

Sample 7 "fassaite"

		Fe	Na	Mg	Al	Si	Ca	Ti
OX	OX	4.57	0.01	12.50	12.06	43.70	25.64	1.00
FM	FM	0.143	0.000	0.698	0.532	1.636	1.028	0.000

Conclusion: fassaite

Total 99.48
4.064

Standards used for microprobe analysis:

For each sample, a Di65Jd35 standard was used for the cations Na, Mg, Al, Si, and Ca. A cossyrite standard was used for Fe and Ti.

Table 9

Table 9 shows the mineralogy of the twelve samples prepared for laboratory reflectance spectra measurements. In the cases of MM1, MM2, and MM8, the proportions of the component phases were predetermined by the results of the norm calculation and the weathering scheme (Table 7a and Figure 6). Other samples prepared as noted.

MM1	olivine + subcalcic augite + fassaite + labradorite + magnetite + ilmenite
MM2	MM1 + kaolinite + anatase + hematite + calcite + quartz
MM3	fassaite + hematite [10:1]
MM4	wollastonite
MM5	olivine + subcalcic augite [5:1]
MM6	subcalcic augite + salite [1:1]
MM7	MM6 + olivine + Ti-magnetite [1:1:1]
MM8	MM2 - MM1
MM9	olivine + subcalcic augite [5:1]
MM10	MM6 + obsidian + Ti-magnetite [1:1:1]
MM11	MM6 + wollastonite [1:1:1]
MM12	fassaite

Table 10

This is a brief tabulation of the features which we believe to be truly present in the laboratory spectra. The features are each labelled with the Figure numbers in which they may be most clearly observed, and a tentative identification according to McCord et al. (1977a), Burns (1970), or Adams (1975).

H_2O bands, 1.35 μm, 1.88 μm, and 2.10 μm: all spectra
Fe^{2+} - Fe^{3+} charge transfer, 0.75-0.85 μm: Figs. 15a,b, 17a

olivine compound feature, 1.00 μm	: Fig. 15a,c(?), 16a,b, 17c
"flattening"; multiple clinopyroxene absorptions, 0.80-0.95 μm	: Fig. 15a, 17a
clinopyroxene "2 μm" feature	: Figs. 16a,b, 17a, 18b

Table 11

Here we list the most important reproducible features of the remotely-sensed reflectance spectra of Mars, after the treatment of McCord et al. (1977a). It cannot be sufficiently stressed that this thesis does not attempt to duplicate the measured spectra of Mars. We simply employ the most obvious spectral evidence possible as a means of distinguishing between alternative modal mineralogies when possible. (Table 11 appears on the next page)

The comparison symbols and lowercase letters at the right of the Table indicate the relative intensities of the features in the spectra labelled a,b, and c in Figure 21.

Table 11

shortward of 0.60 μm, intense absorption	: Fig. 21;	a≃b≃c
feature centered near 0.81 μm	: Fig. 21;	a≃b≃c
"check-mark" feature at 0.87 μm	: Fig. 21;	c>b>a
smooth "check-mark" feature, 0.97 μm	: Fig. 21;	a>c>b

Figure Captions

Figure 1 has been deleted

Figure 2 S-1 Sample Acquisition Data

Figure 3 Primary Phases and Their Weathering Product Phases

Figure 4 Sequence of Steps in Modified Normative Procedure

Figure 5 Pyroxene Field with Microprobe Samples Superimposed by Number

Figure 6 Primary-to-Weathered Phase Chart with Weight Per Cent Proportions

Figure 7 P-T Relations for Several Important Rock Types

Figure 8 Phase Relations for Liquids in System Ne-Fo-CaTs-Qz

Figure 9 Basalt Flow Diagram (this and Figure 8: Yoder, 1976a)

Figure 10 Olivine Phase System (Yoder, 1976a)

Figure 11 Pyroxene Spectra (McCord et al., 1977a)

Figure 12 Feldspar Spectra (McCord et al., 1977a)

Figures 13a,b Olivine and Glass Spectra (McCord et al., 1977a)

Figure 14 Anorthite Enrichment by Partial Melting, System Di-Ab-An

Figures 15a,b,c Laboratory Spectra: MM1, MM2, MM8

Figures 16a,b Laboratory Spectra: MM5 and MM9

Figures 17a,b,c,d Laboratory Spectra:MM6, MM 11, MM7, and MM10

Figures 18a,b Laboratory Spectra: MM12, MM3

Figure 19 Laboratory Spectrum: MM4

Figure 20 Iron Oxide Spectra (McCord et al., 1977a)

Figure 21 Dark Area Telescopic Spectra (McCord et al., 1977a)

Figure 22 Band-Band Plot for Several Important Minerals (McCord et al., 1977a)

Figure 2

Sample VL-1, S-1: acquisitions 1 and 2

Drift deposit of eolian sediment
Sampled from 4-6 cm below the surface
Grain sizes fine, 2 mm
Acquired sol 8, hour 10:46 to 11:43

Figure 3

Primary Phase	Weathering Product Phases
olivine	montmorillonite, Fe_2O_3, SiO_2
clinopyroxene	montmorillonite, Fe_2O_3, $CaCO_3$
albite	kaolinite
anorthite	kaolinite, $CaCO_3$
orthoclase	kaolinite
magnetite	Fe_2O_3
ilmenite	Fe_2O_3, TiO_2

Figure 4

Within the standard normative mineralogy of Cross, Iddings, Pierson and Washington (C.I.P.W.), we select only those steps which involve exclusively the component oxides listed in Table 6:

1) ilmenite
2) provisional orthoclase
3) provisional albite
4) anorthite
5) magnetite
6) provisional diopside; Mg/Fe ratio is fixed
7) silica is added in proportion, 2,3,4,6
8) hypersthene/olivine balance

Figure 6

	$Mg_3Si_2O_5(OH)_4$	$Al_2Si_2O_5(OH)_4$	TiO_2	Fe_2O_3	$CaCO_3$	SiO_2
$Mg_{1.12}Fe_{0.88}SiO_4$	0.3990	—	—	0.1756	—	0.1995
$CaMg_{0.56}Fe_{0.44}Si_2O_6$	0.0529	—	—	0.0416	0.0945	—
$NaAlSi_3O_8$	—	0.0922	—	—	—	—
$CaAl_2Si_2O_8$	—	0.0178	—	—	0.0178	—
$KAlSi_3O_8$	—	0.0102	—	—	—	—
Fe_3O_4	—	—	—	0.0375	—	—
$FeTiO_3$	—	—	0.0208	0.0104	—	—
Total	0.4519	0.1202	0.0208	0.2651	0.1123	0.1995
Weight Percent	38.63	10.27	1.78	22.66	9.60	17.05

(69)

Figure 5

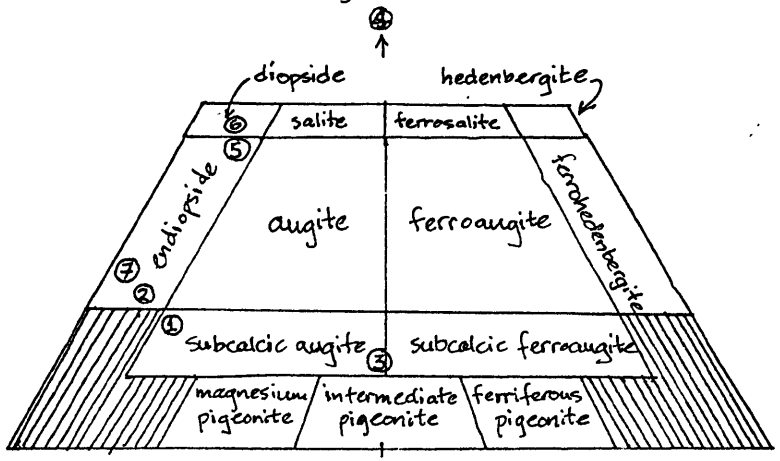

Figure 7

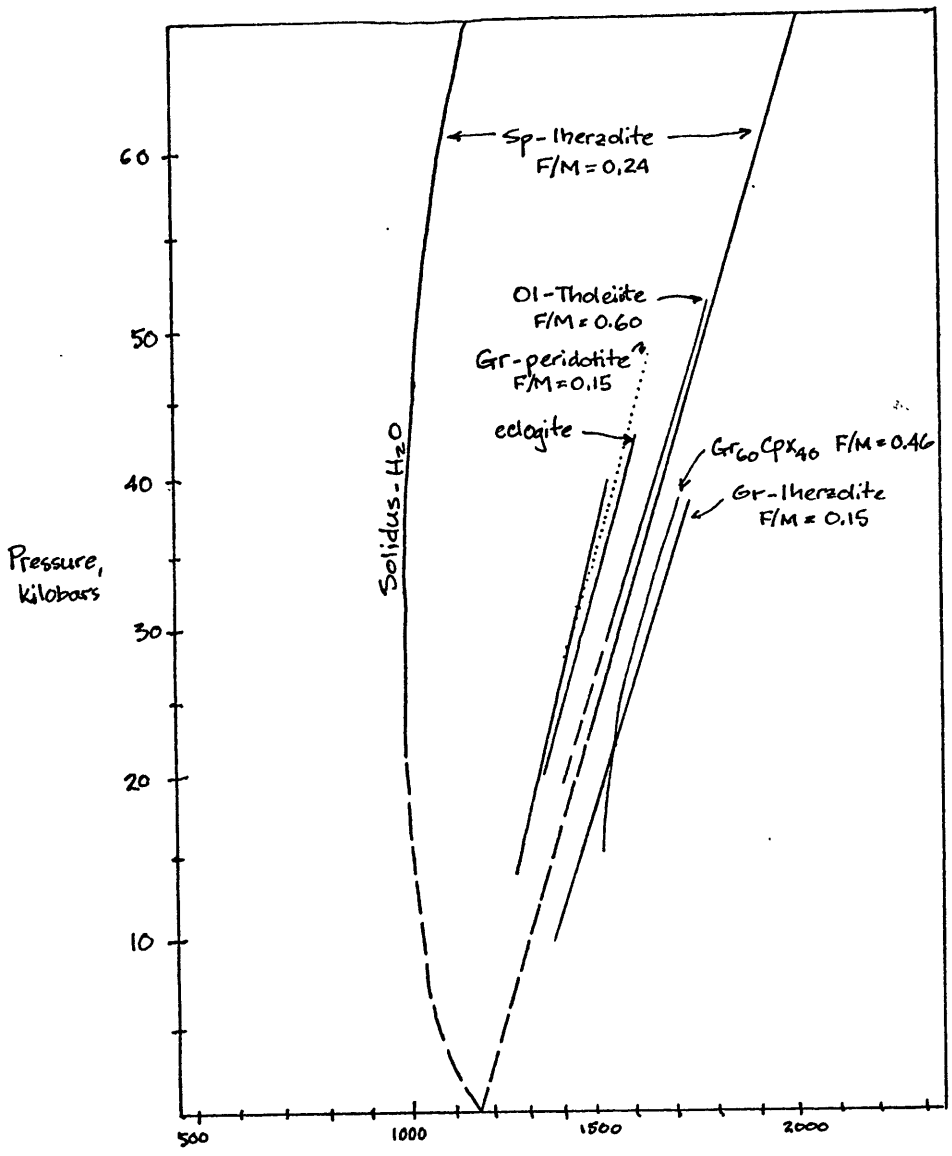

F/M = FeO/FeO + MgO

[after Yoder, 1976a, Fig. 8-4

Figure 8

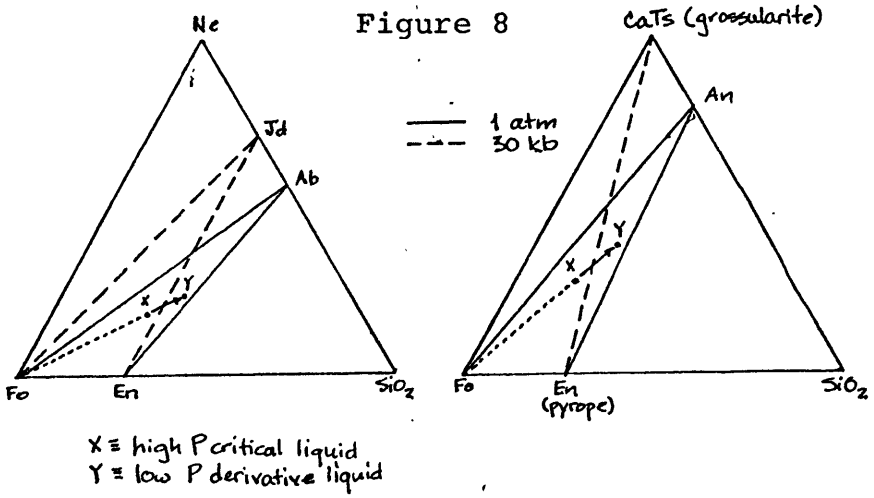

X ≡ high P critical liquid
Y ≡ low P derivative liquid

Figure 9

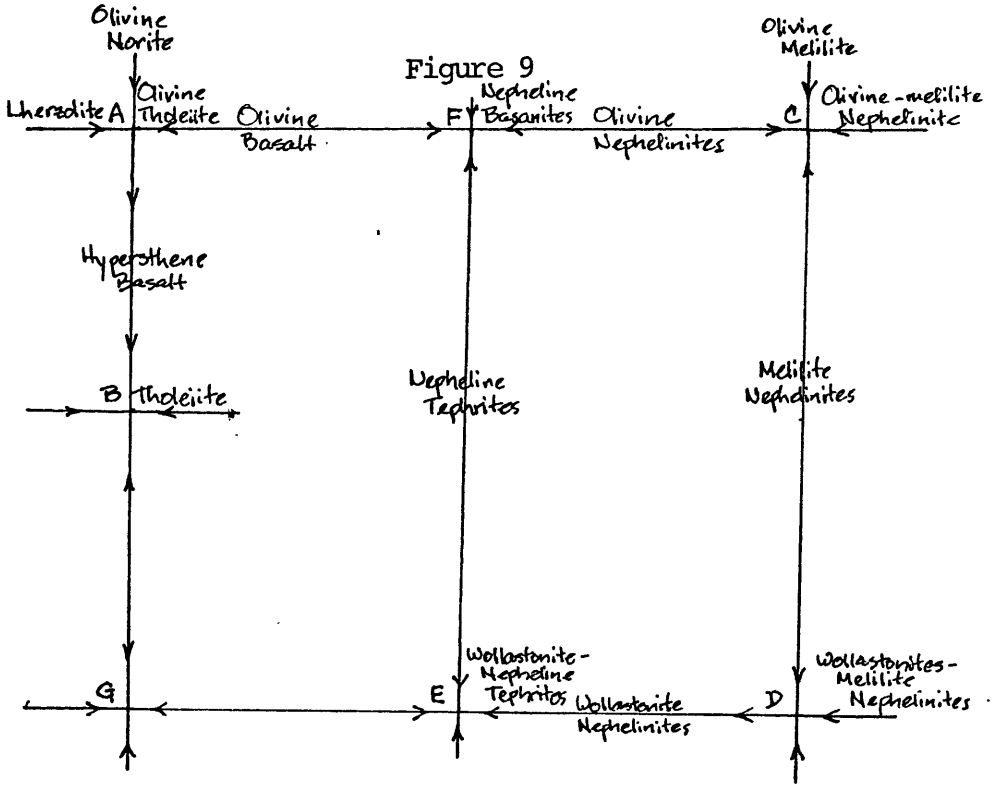

Figure 10

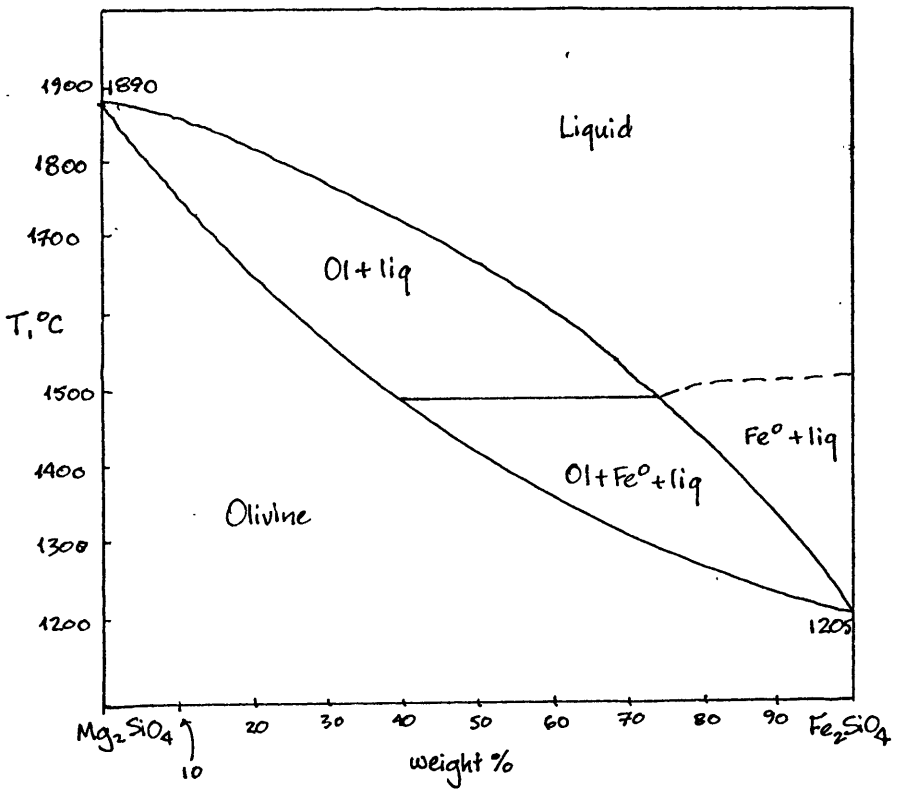
1900
1890
1800
1700
T, °C
1500
1400
1300
1200
Liquid
Ol + liq
Fe° + liq
Ol + Fe° + liq
Olivine
1205
Mg2SiO4
10
20
30
40
50
60
70
80
90
Fe2SiO4
weight %

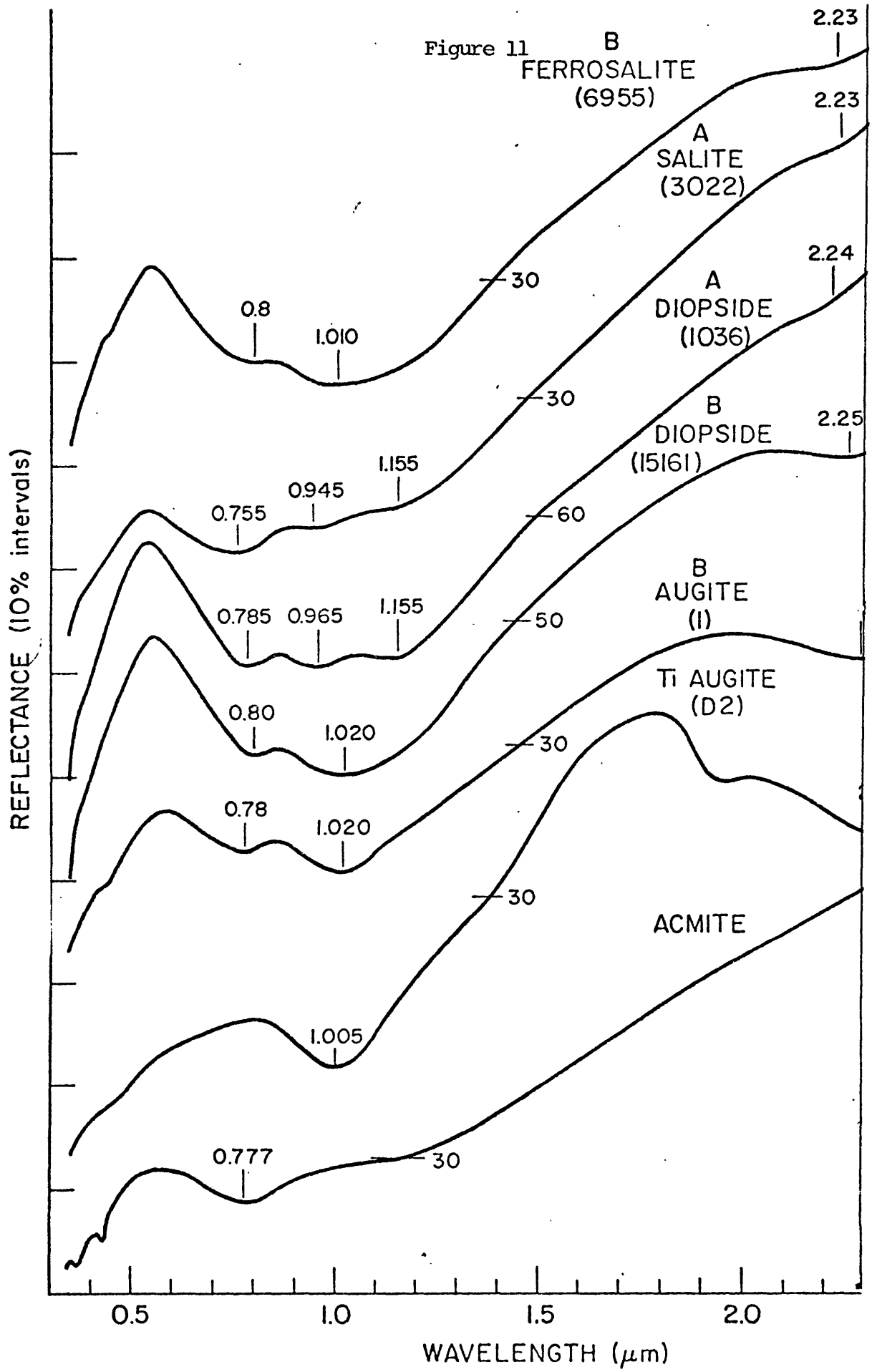
B
FERROSALITE
(6955)
2.23
A
SALITE
(3022)
2.23
A
DIOPSIDE
(1036)
2.24
B
DIOPSIDE
(15161)
2.25
B
AUGITE
(1)
Ti AUGITE
(D2)
ACMITE
0.8
1.010
30
0.755
0.945
1.155
30
0.785
0.965
1.155
60
0.80
1.020
50
0.78
1.020
30
1.005
30
0.777
30
REFLECTANCE (10% intervals)
0.5
1.0
1.5
2.0
WAVELENGTH (μm)

Figure 11

Figure 12

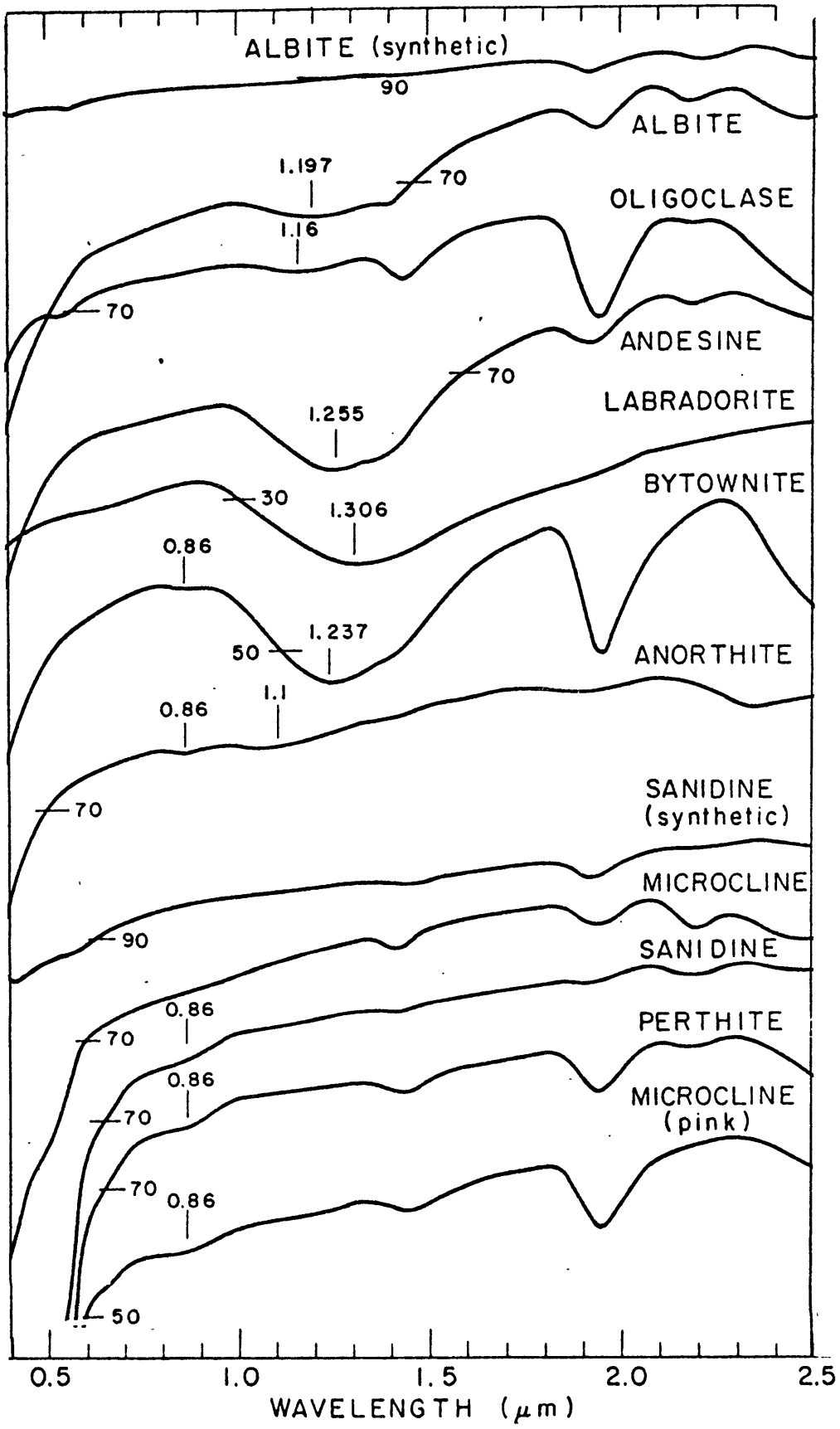
ALBITE (synthetic)
90
ALBITE
1.197
70
OLIGOCLASE
1.16
70
ANDESINE
70
LABRADORITE
1.255
BYTOWNITE
30
1.306
0.86
1.237
50
ANORTHITE
0.86
1.1
70
SANIDINE
(synthetic)
MICROCLINE
90
SANIDINE
0.86
70
PERTHITE
0.86
70
MICROCLINE
(pink)
70
0.86
50
0.5
1.0
1.5
2.0
2.5
WAVELENGTH (μm)

Figure 13a

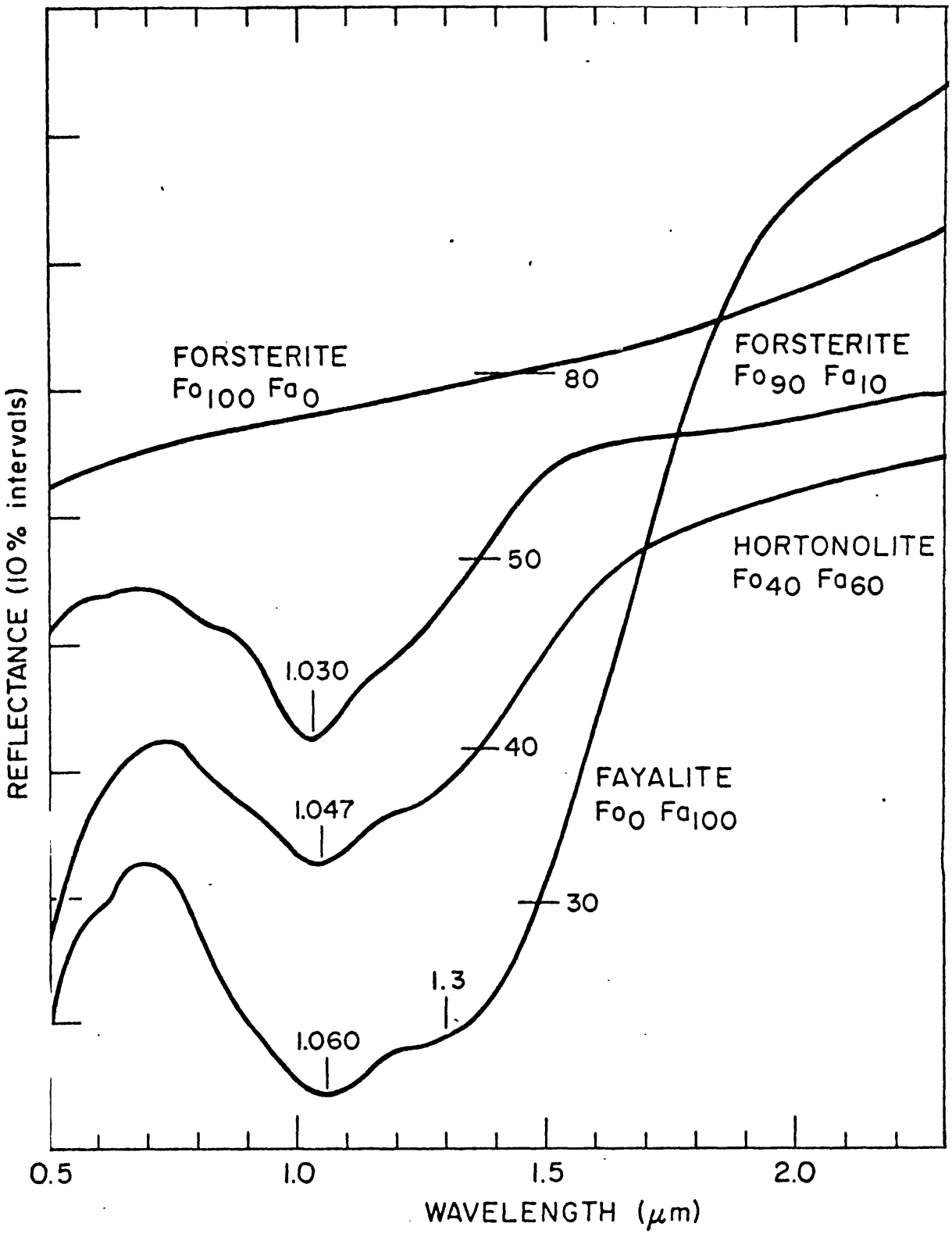
FORSTERITE
Fo100 Fa0
80
FORSTERITE
Fo90 Fa10
50
HORTONOLITE
Fo40 Fa60
1.030
40
FAYALITE
Fo0 Fa100
1.047
30
1.3
1.060
REFLECTANCE (10% intervals)
0.5
1.0
1.5
2.0
WAVELENGTH (μm)

Figure 13b

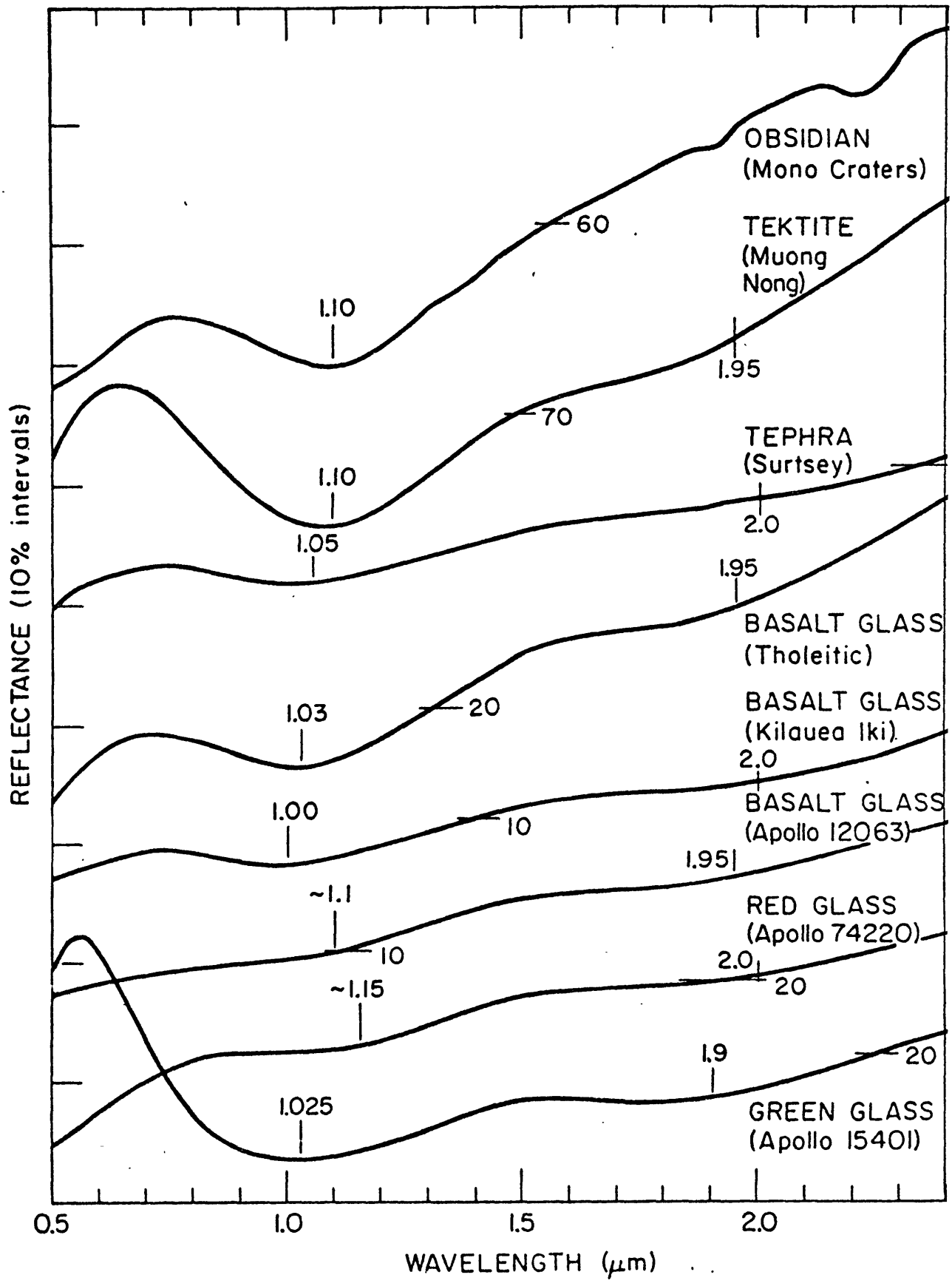
OBSIDIAN
(Mono Craters)
60
1.10
TEKTITE
(Muong
Nong)
1.95
70
1.10
TEPHRA
(Surtsey)
2.0
1.05
1.95
BASALT GLASS
(Tholeitic)
1.03
20
BASALT GLASS
(Kilauea Iki)
2.0
1.00
10
BASALT GLASS
(Apollo 12063)
1.95
~1.1
RED GLASS
(Apollo 74220)
10
2.0
~1.15
20
1.9
20
1.025
GREEN GLASS
(Apollo 15401)
REFLECTANCE (10% intervals)
0.5
1.0
1.5
2.0
WAVELENGTH (μm)

Figure 14

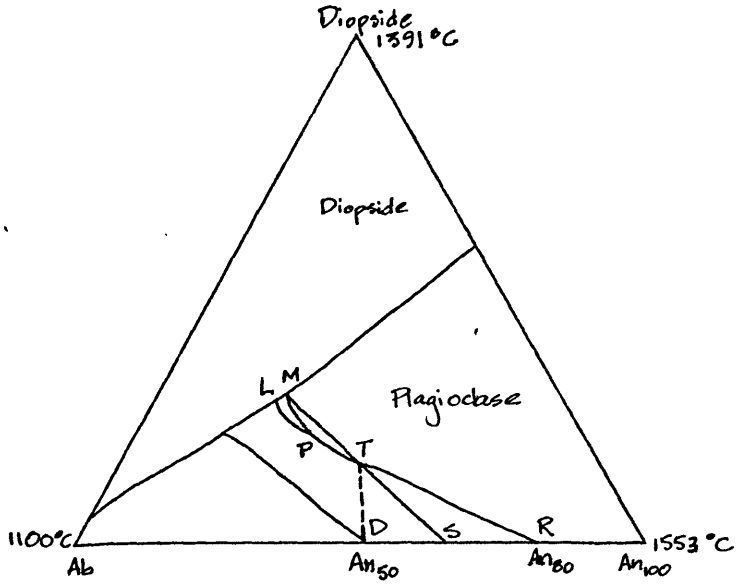
Diopside
1391°C
Diopside
L
M
Plagioclase
P
T
D
S
R
1100°C
1553°C
Ab
An50
An80
An100

Figure 15

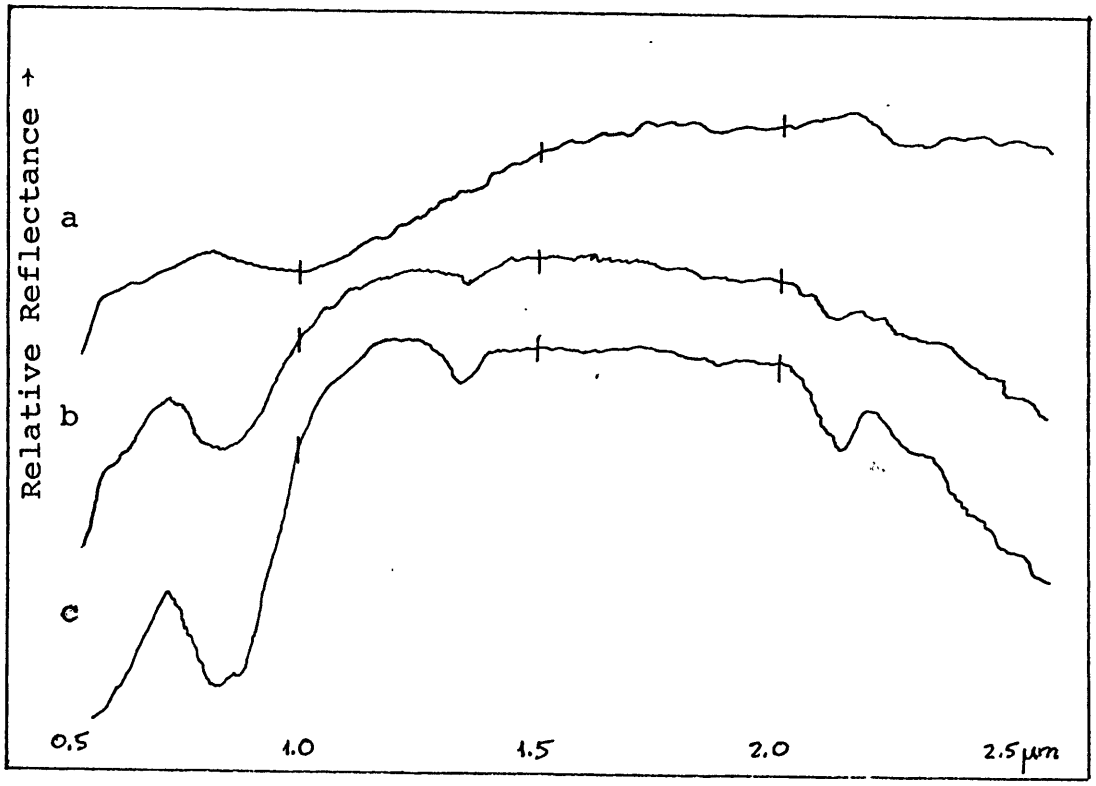

Figure 16

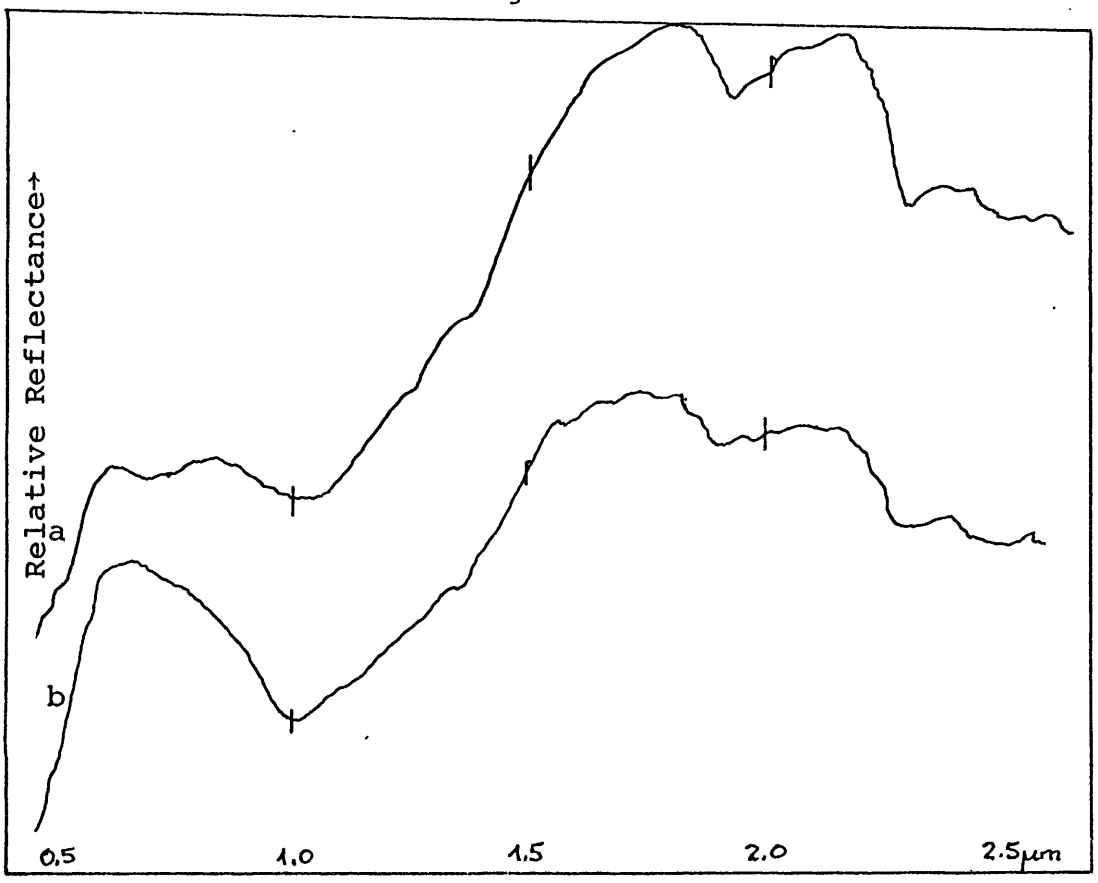

Figure 17

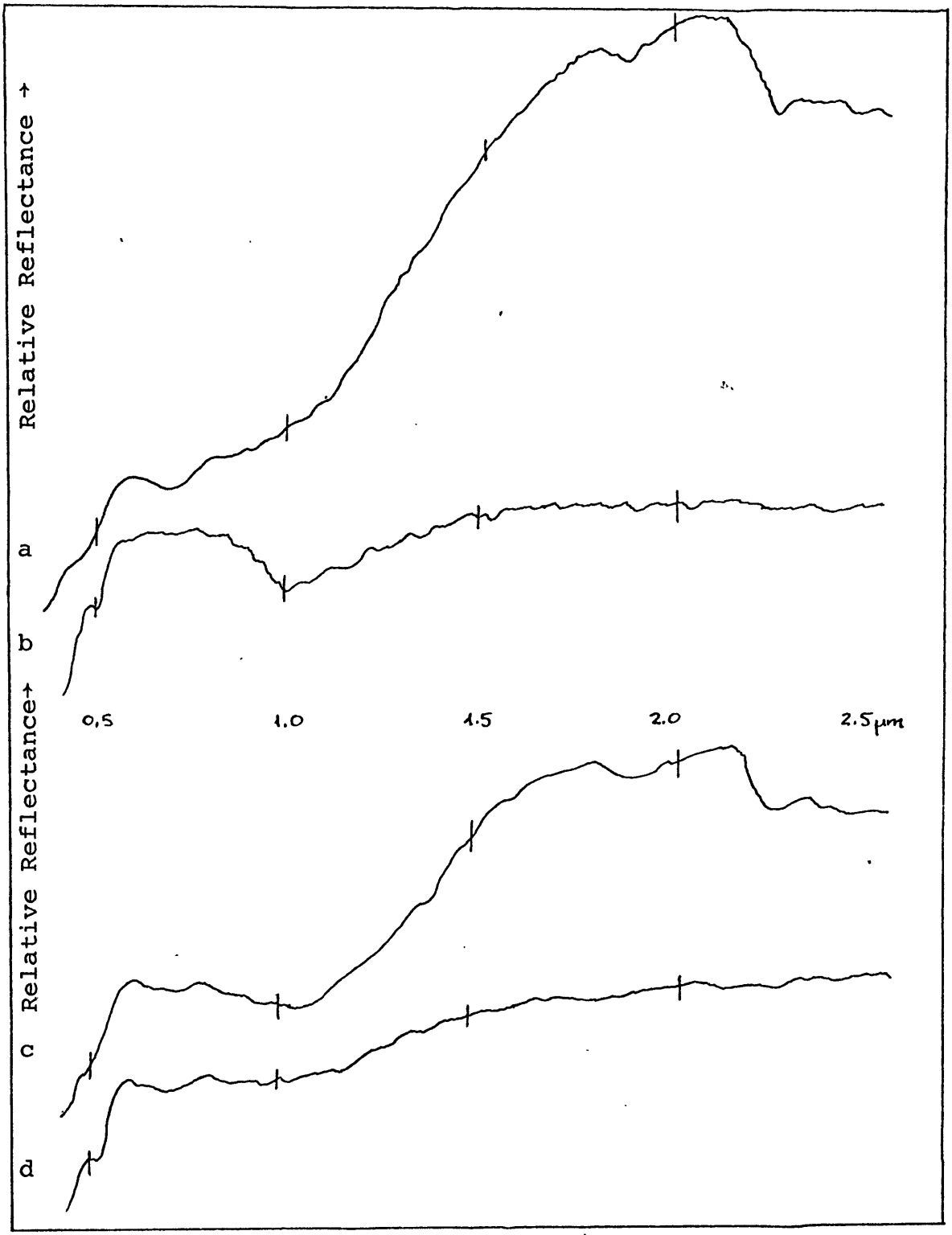
Relative Reflectance →
a
b
0.5
1.0
1.5
2.0
2.5μm
Relative Reflectance→
c
d

Figure 18

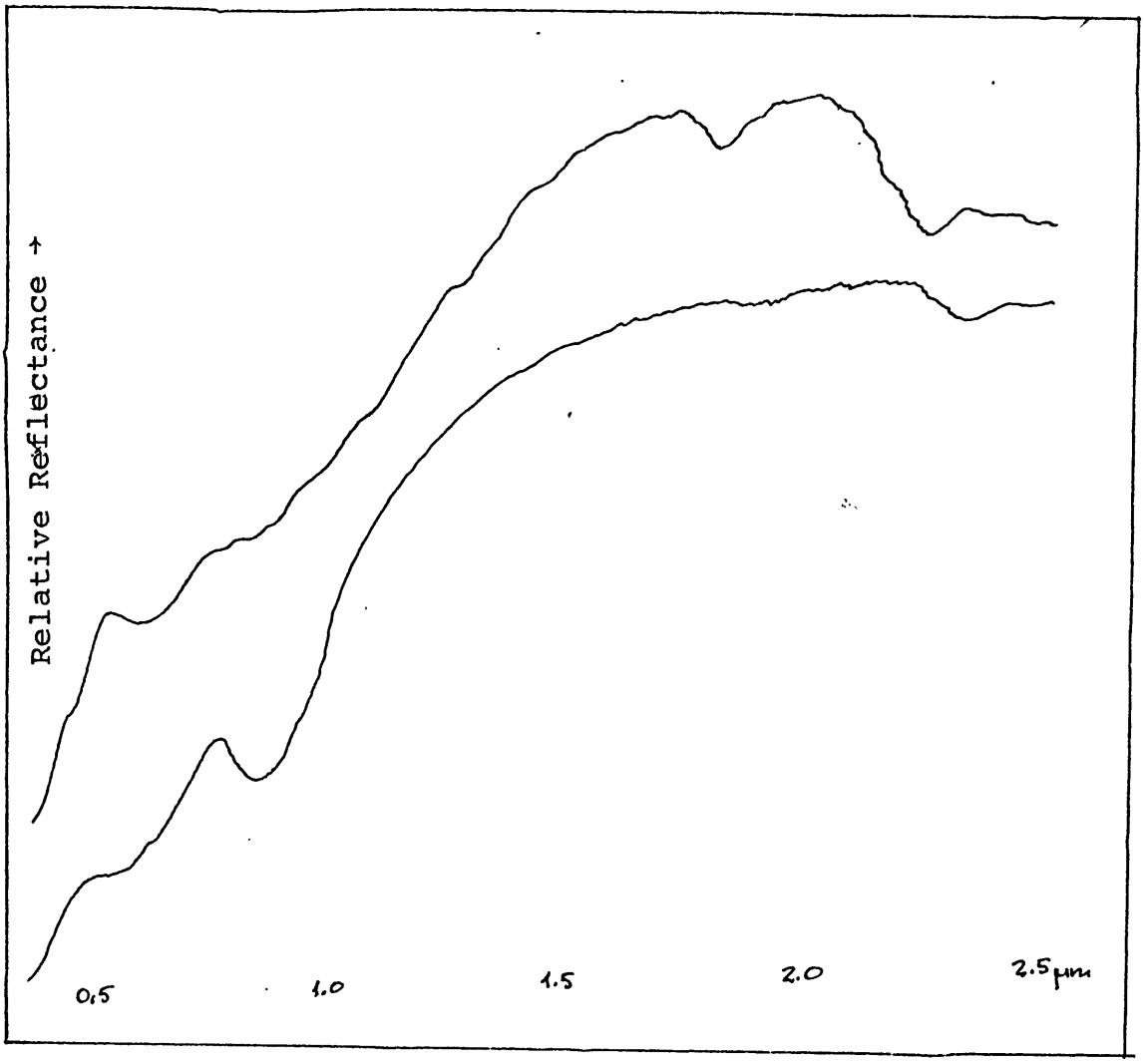

Figure 19

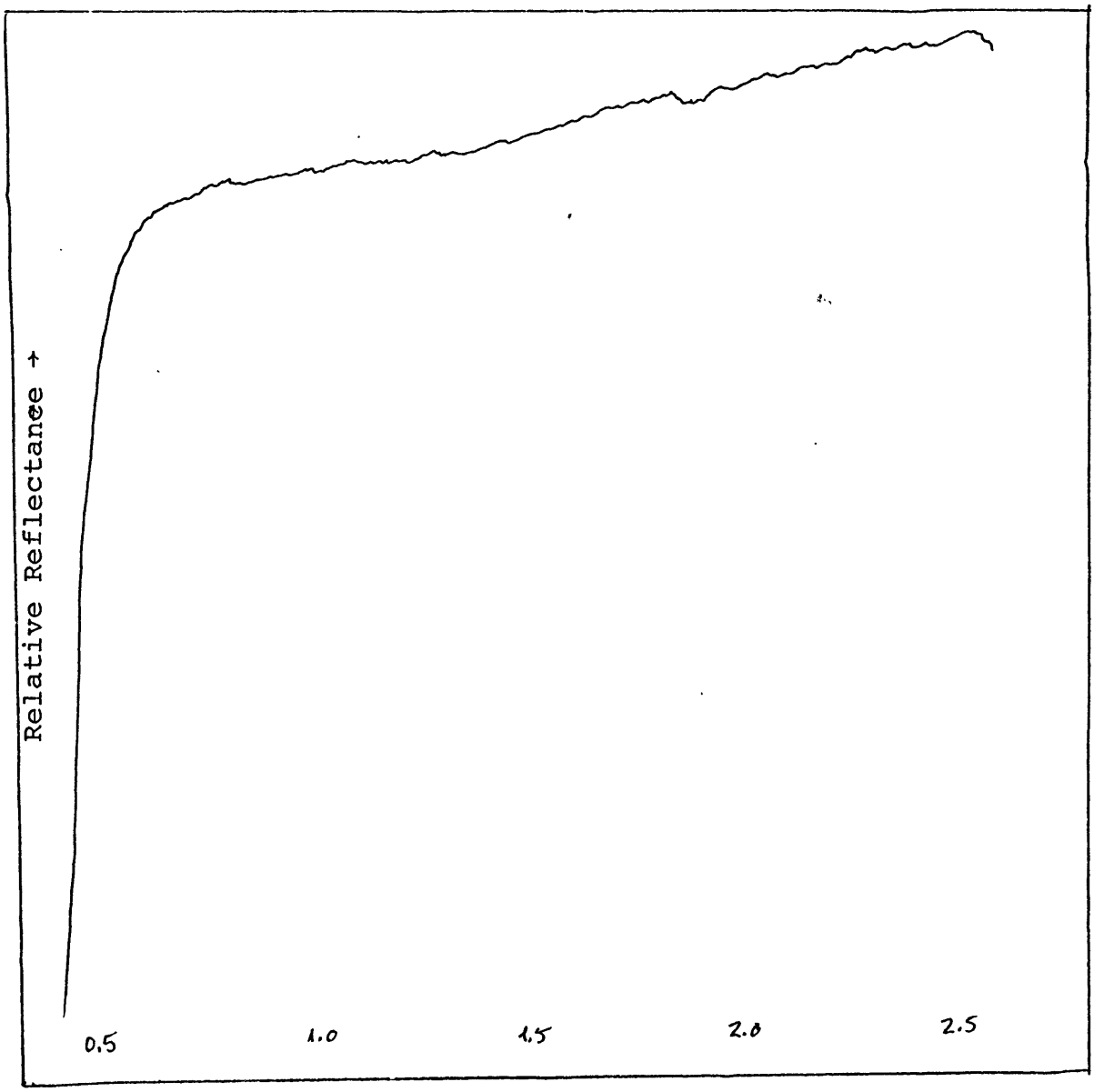

Figure 20

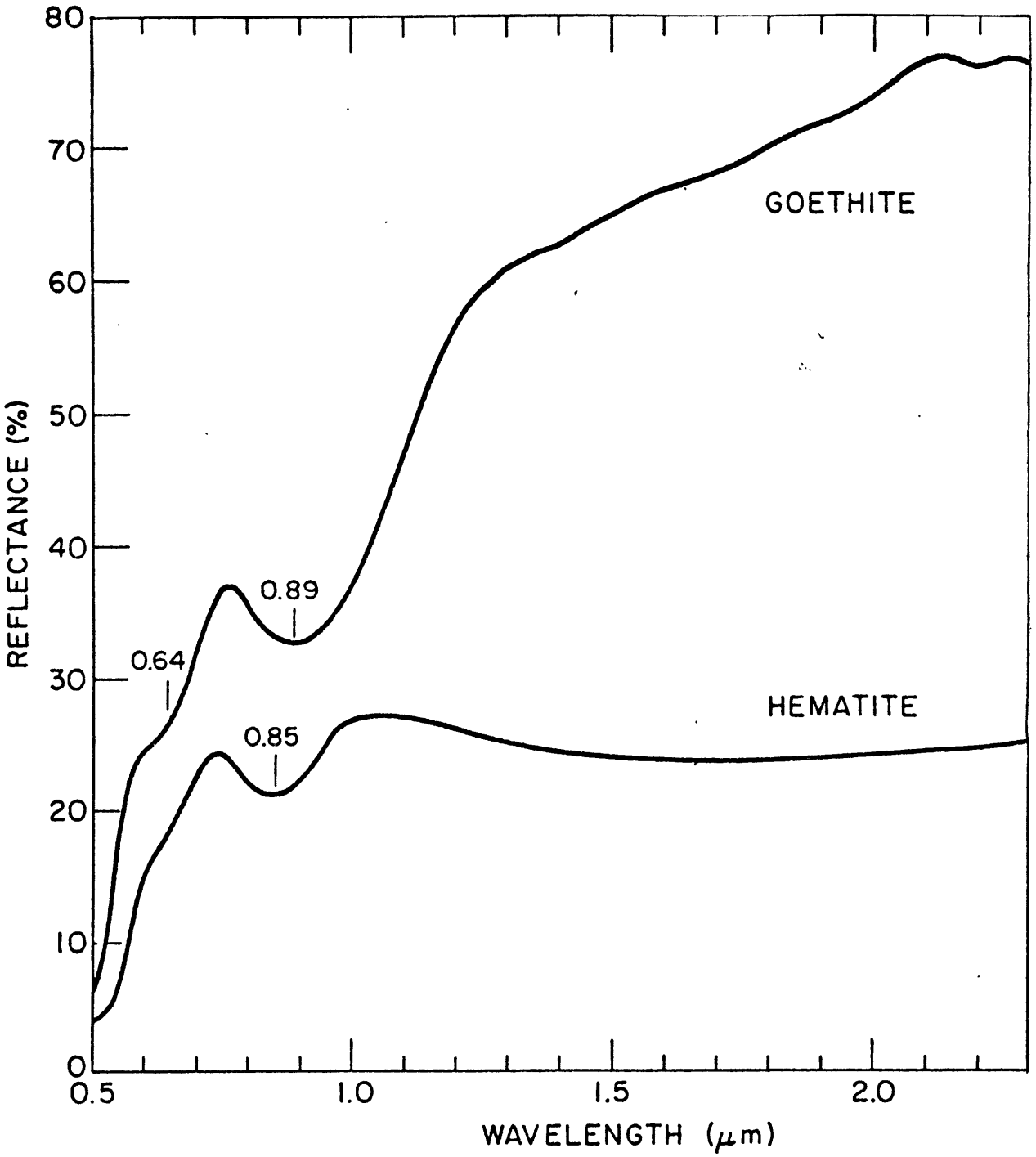
80
70
60
50
40
30
20
10
0
REFLECTANCE (%)
GOETHITE
HEMATITE
0.64
0.89
0.85
0.5
1.0
1.5
2.0
WAVELENGTH (μm)

Figure 21

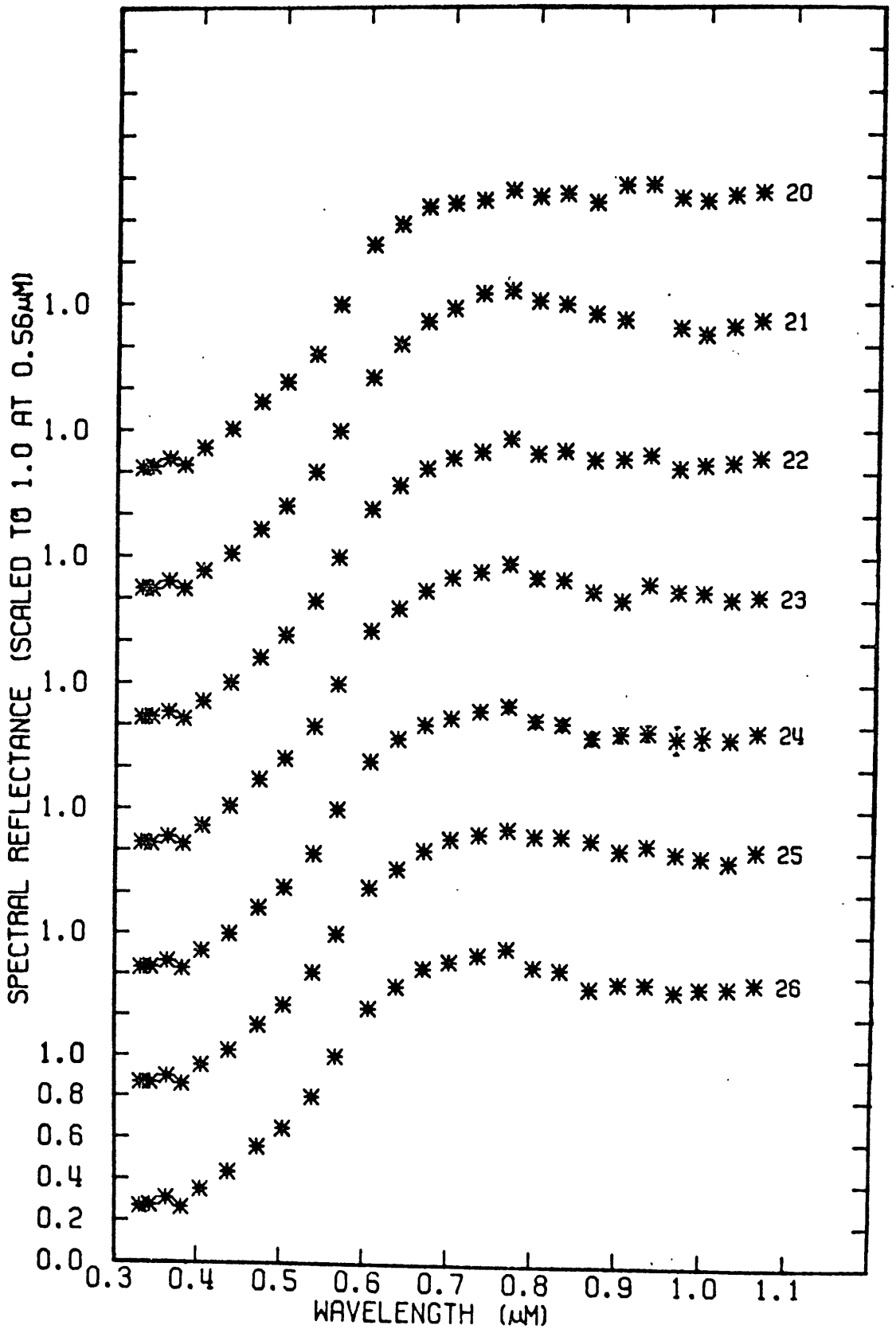
SPECTRAL REFLECTANCE (SCALED TO 1.0 AT 0.56μM)
1.0
1.0
1.0
1.0
1.0
1.0
1.0
0.8
0.6
0.4
0.2
0.0
0.3
0.4
0.5
0.6
0.7
0.8
0.9
1.0
1.1
WAVELENGTH (μM)
20
21
22
23
24
25
26

Figure 22

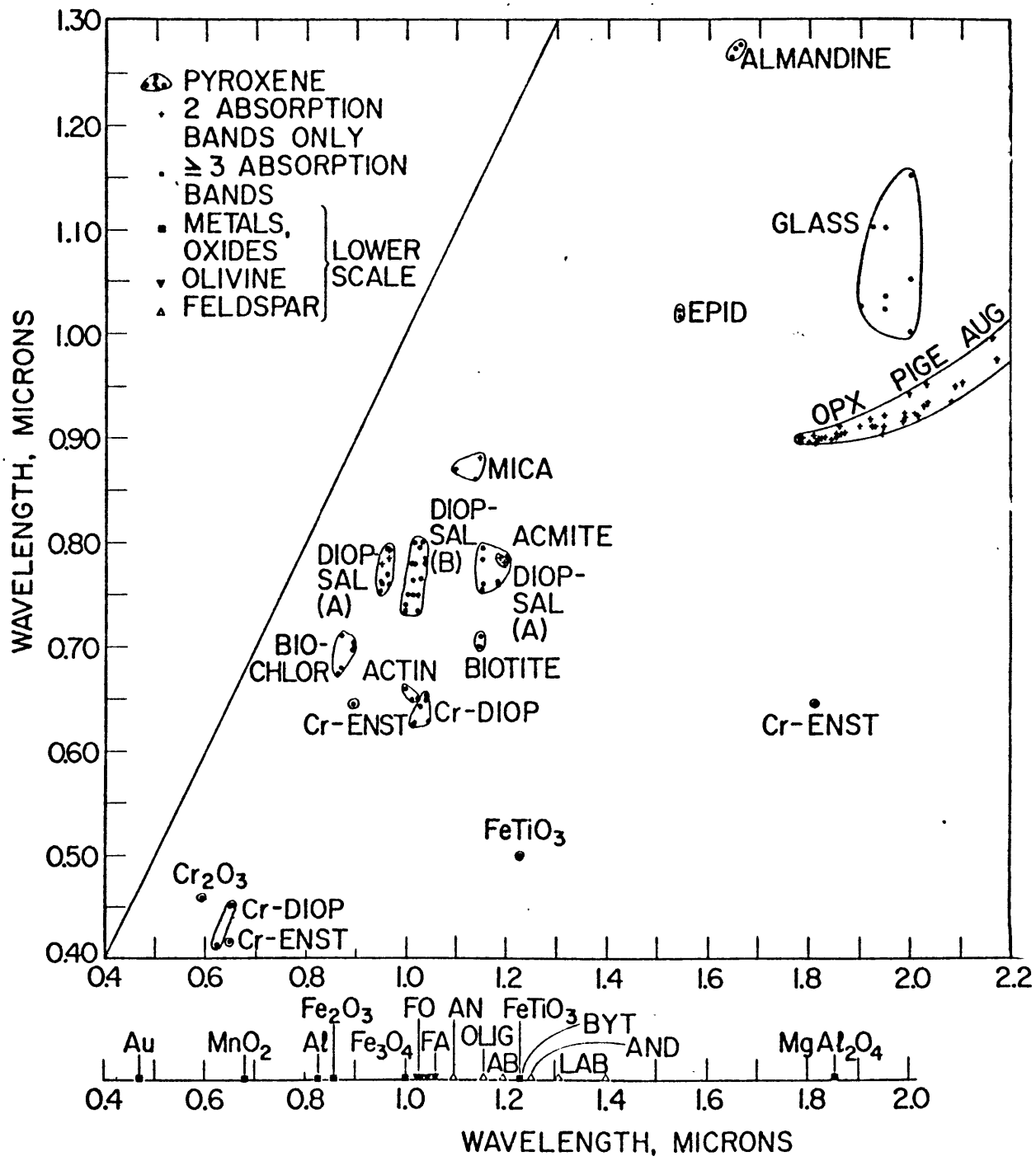
PYROXENE
2 ABSORPTION BANDS ONLY
≥ 3 ABSORPTION BANDS
METALS, OXIDES
OLIVINE
FELDSPAR
LOWER SCALE
ALMANDINE
GLASS
EPID
OPX
PIGE
AUG
MICA
DIOP-SAL (B)
ACMITE
DIOP-SAL (A)
DIOP-SAL (A)
BIO-CHLOR
ACTIN
BIOTITE
Cr-ENST
Cr-DIOP
Cr-ENST
FeTiO3
Cr2O3
Cr-DIOP
Cr-ENST
WAVELENGTH, MICRONS
Fe2O3
FO
AN
FeTiO3
BYT
Au
MnO2
Al
Fe3O4
FA
OLIG
AND
AB
LAB
MgAl2O4
WAVELENGTH, MICRONS